ELSEVIER

Impact of 1/8° to 1/64° resolution on Gulf Stream model–data comparisons in basin-scale subtropical Atlantic Ocean models

Harley E. Hurlburt [*], Patrick J. Hogan

Naval Research Laboratory, Stennis Space Center, MS 39529-5004, USA

Abstract

We investigate the impact of 1/8°, 1/16°, 1/32°, and 1/64° ocean model resolution on model–data comparisons for the Gulf Stream system mainly between the Florida Straits and the Grand Banks. This includes mean flow and variability, the Gulf Stream pathway, the associated nonlinear recirculation gyres, the large-scale C-shape of the subtropical gyre and the abyssal circulation. A nonlinear isopycnal, free surface model covering the Atlantic from 9°N to 47°N or 51°N, including the Caribbean and Gulf of Mexico, and a similar 1/16° global model are used. The models are forced by winds and by a global thermohaline component via ports in the model boundaries. When calculated using realistic wind forcing and Atlantic model boundaries, linear simulations with Munk western boundary layers and a Sverdrup interior show two unrealistic mean Gulf Stream pathways between Cape Hatteras and the Grand Banks, one proceeding due east from Cape Hatteras and a second one continuing northward along the western boundary until forced eastward by the regional northern boundary. The northern pathway is augmented when a linear version of the upper ocean global thermohaline contribution to the Gulf Stream is added as a Munk western boundary layer. A major change is required to obtain a realistic pathway in nonlinear models. Resolution of 1/8° is eddy-resolving but mainly gives a wiggly version of the linear model Gulf Stream pathway and weak abyssal flows except for the deep western boundary current (DWBC) forced by ports in the model boundaries. All of the higher resolution simulations show major improvement over the linear and 1/8° nonlinear simulations. Additional major improvement is seen with the increase from 1/16° to 1/32° resolution and modest improvement with a further increase to 1/64°. The improvements include (1) realistic separation of the Gulf Stream from the coast at Cape Hatteras and a realistic Gulf Stream pathway between Cape Hatteras and the Grand Banks based on comparisons with Gulf Stream pathways from satellite IR

---

[*] Corresponding author. Tel.: +1-228-688-4626; fax: +1-228-688-4759.
E-mail address: hurlburt@nrlssc.navy.mil (H.E. Hurlburt).

Report Documentation Page

Public reporting burden for the collection of information is estimated to average 1 hour per response, including the time for reviewing instructions, searching existing data sources, gathering and maintaining the data needed, and completing and reviewing the collection of information. Send comments regarding this burden estimate or any other aspect of this collection of information, including suggestions for reducing this burden, to Washington Headquarters Services, Directorate for Information Operations and Reports, 1215 Jefferson Davis Highway, Suite 1204, Arlington VA 22202-4302. Respondents should be aware that notwithstanding any other provision of law, no person shall be subject to a penalty for failing to comply with a collection of information if it does not display a currently valid OMB control number.

1. REPORT DATE **30 APR 1999**	2. REPORT TYPE	3. DATES COVERED **00-00-1999 to 00-00-1999**

4. TITLE AND SUBTITLE **Impact of 1/8 degree to 1/64 degree resolution on Gulf Stream model-data comparisons in basin-scale subtropical Atlantic Ocean models**	5a. CONTRACT NUMBER
	5b. GRANT NUMBER
	5c. PROGRAM ELEMENT NUMBER
6. AUTHOR(S)	5d. PROJECT NUMBER
	5e. TASK NUMBER
	5f. WORK UNIT NUMBER
7. PERFORMING ORGANIZATION NAME(S) AND ADDRESS(ES) **Naval Research Laboratory,Oceanographic Division,Stennis Space Center,MS,39529-5004**	8. PERFORMING ORGANIZATION REPORT NUMBER
9. SPONSORING/MONITORING AGENCY NAME(S) AND ADDRESS(ES)	10. SPONSOR/MONITOR'S ACRONYM(S)
	11. SPONSOR/MONITOR'S REPORT NUMBER(S)

12. DISTRIBUTION/AVAILABILITY STATEMENT
Approved for public release; distribution unlimited

13. SUPPLEMENTARY NOTES

14. ABSTRACT
see report

15. SUBJECT TERMS

16. SECURITY CLASSIFICATION OF:			17. LIMITATION OF ABSTRACT	18. NUMBER OF PAGES	19a. NAME OF RESPONSIBLE PERSON
a. REPORT **unclassified**	b. ABSTRACT **unclassified**	c. THIS PAGE **unclassified**	**Same as Report (SAR)**	**47**	

and from GEOSAT and TOPEX/Poseidon altimetry (but $1/32°$ resolution was required for robust results), (2) realistic eastern and western nonlinear recirculation gyres (which contribute to the large-scale C-shape of the subtropical gyre) based on comparisons with mean surface dynamic height from the generalized digital environmental model (GDEM) oceanic climatology and from the pattern and amplitude of sea surface height (SSH) variability surrounding the eastern gyre as seen in TOPEX/Poseidon altimetry, (3) realistic upper ocean and DWBC transports based on several types of measurements, (4) patterns and amplitude of SSH variability which are generally realistic compared to TOPEX/Poseidon altimetry, but which vary from simulation to simulation for specific features and which are most realistic overall in the $1/64°$ simulation, (5) a basin wide explosion in the number and strength of mesoscale eddies (with warm core rings (WCRs) north of the Gulf Stream, the regional eddy features best observed by satellite IR), (6) realistic statistics for WCRs north of the Gulf Stream based on comparison to IR analyses (low at $1/16°$ resolution and most realistic at $1/64°$ resolution for mean population and rings generated/year; realistic ring diameters at all resolutions), and (7) realistic patterns and amplitude of abyssal eddy kinetic energy (EKE) in comparison to historical measurements from current meters. Published by Elsevier Science B.V.

1. Introduction

This paper is part of a collection for a special issue on the project Data Assimilation and Model Evaluation Experiment — North Atlantic Basin (DAMÉE-NAB). This contribution focuses on the impact of numerical model resolution on ocean model agreement with observations in the Gulf Stream region between the Florida Straits and the Grand Banks. That includes the mean flow and variability, the Gulf Stream pathway, the associated nonlinear recirculation gyres, the large-scale C-shape of the subtropical gyre, and the abyssal circulation.

Linear solutions forced by different wind sets (Townsend et al., 2000, this issue) each give two unrealistic Gulf Stream pathways between Cape Hatteras and the Grand Banks, one extending eastward from Cape Hatteras and a second one continuing northward along the western boundary until forced eastward by a northern boundary segment, which extends eastward to the Grand Banks. The second pathway is augmented by a linear version of the upper ocean global thermohaline contribution to the Gulf Stream. Dynamically, these linear simulations are essentially the same as Munk (1950) with a Sverdrup (1947) interior done with realistic wind forcing and model boundaries, including islands. The global thermohaline component is included as a Munk western boundary layer via open ports in the model boundaries.

A major change is required to get from the two linear Gulf Stream pathways to a realistic nonlinear pathway between Cape Hatteras and the Grand Banks. Accomplishing this has been a challenging problem to ocean modelers, with nonlinear, eddying simulations typically showing overshoot of the observed latitude for Gulf Stream separation from the coast and/or some wiggly representation of the linear solution pathways (Bryan et al., 1995; Dengg et al., 1996; DYNAMO Group, 1997). Is it possible to make nonlinear numerical models simulate realistic Gulf Stream pathways

simply by increasing the grid resolution? If so, what model resolution is required to give realistic nonlinear simulations in comparison to observations? Do we see simulation convergence for the mean flow and the statistics of the variability as the resolution is increased and the eddy viscosity is decreased, as permitted by each resolution increase? Addressing these issues in the context of model–data comparisons is the focus of this paper. Model dynamics for the Gulf Stream system, including the effects of model resolution, will be the subject of a separate paper.

In the numerical simulations used here, the model resolution ranges from $1/8°$ (14 km) to $1/64°$ (1.8 km) for each model variable with five or six layers in the vertical. In most cases, the model domain covers the Atlantic from 9°N to 47°N or 51°N, including the Caribbean and the Gulf of Mexico, but a $1/16°$ global model is also used for comparison. The global thermohaline contribution, upper ocean and deep western boundary current (DWBC), is included via ports in the model boundaries. Additional information on the ocean model and the design of the numerical simulations is provided in Sections 2 and 3, respectively. The results are presented in Sections 4–7 and a summary and the conclusions are in Section 8.

2. The ocean model

The numerical simulations were performed using the Naval Research Laboratory (NRL) layered ocean model (NLOM), a descendent of the semi-implicit, free surface model by Hurlburt and Thompson (1980), but with greatly expanded capability (Wallcraft, 1991). Moore and Wallcraft (1998) detail the mathematical and numerical formulation in spherical coordinates with attention to the proper formulation of isopycnal diffusion, which preserves solid body rotation. Wallcraft and Moore (1997) discuss the development of a scalable, portable version of NLOM. This version runs efficiently and interchangeably on a wide variety of computer architectures using a tiled data parallel programming paradigm. This approach is general enough that the technique used to obtain scalability on a given computer system can be selected at compile time from (1) data parallel, (2) message passing, (3) autotasking or (4) message passing between multi-processor autotasked systems. For example, the model has run on workstations, the HP/Convex Exemplar SPP2000, the Cray C90, J90, T3D, T3E, T90 and YMP, the IBM SP, the SGI PCA and Origin 2000, and the Thinking Machines CM5.

At $1/32°$ resolution, the grid size is $2048 \times 1344 \times 5$ for an Atlantic–Caribbean–Gulf of Mexico domain covering 9°N–51°N. At this resolution, the model was typically run using 56 processing elements on a Cray T3E-900 and required 20.4 wall clock h/model year with a time step of 6 min. This timing includes all the typical I/O and sampling of the model output. See Wallcraft (1998) for an extensive table of timings for this $1/32°$ model domain on the Cray T3E-900, the IBM SP, the HP/Convex SPP2000 and the SGI Origin 2000, when the model was run on 14 to 224 processors. Using 56 processors, the timings on the other machines were only 10% to 50% longer than on the Cray T3E-900.

The model is a primitive equation (PE) layered formulation where the model equations have been vertically integrated through each layer and the interfaces between

the layers are isopycnal. The equations for the n-layer finite depth, hydrodynamic model are given below for layers $k = 1 \ldots n$ with $k = 1$ for the top layer. In places where k is used to index model interfaces, $k = 0$ is the surface and $k = n$ is the bottom.

$$\frac{\partial U_k}{\partial t} + \frac{1}{a\cos\theta}\left[\frac{\partial(U_k u_k)}{\partial\phi} + \frac{\partial(V_k u_k\cos\theta)}{\partial\theta} - V_k(u_k\sin\theta + a\Omega\sin2\theta)\right]$$

$$= +\max(0, -\omega_{k-1})u_{k-1} + \max(0, \omega_k)u_{k+1} - (\max(0, -\omega_k)$$

$$+\max(0, \omega_{k-1}))u_k + \max(0, -C_M\omega_{k-1})(u_{k-1} - u_k)$$

$$+\max(0, C_M\omega_k)(u_{k+1} - u_k) - \frac{h_k}{a\cos\theta}\sum_{j=1}^{n}G_{kj}\frac{\partial(h_j - H_j)}{\partial\phi}$$

$$+(\tau_{\phi_{k-1}} - \tau_{\phi_k})/\rho_0 + \frac{A}{a^2\cos^2\theta}\left[\frac{\partial(h_k e_{\phi\phi_k}\cos\theta)}{\partial\phi} + \frac{\partial(h_k e_{\phi\theta_k}\cos^2\theta)}{\partial\theta}\right] \qquad (1)$$

$$\frac{\partial V_k}{\partial t} + \frac{1}{a\cos\theta}\left[\frac{\partial(U_k v_k)}{\partial\phi} + \frac{\partial(V_k v_k\cos\theta)}{\partial\theta} + U_k(u_k\sin\theta + a\Omega\sin2\theta)\right]$$

$$= +\max(0, -\omega_{k-1})v_{k-1} + \max(0, \omega_k)v_{k+1} - (\max(0, -\omega_k)$$

$$+\max(0, \omega_{k-1}))v_k + \max(0, -C_M\omega_{k-1})(v_{k-1} - v_k)$$

$$+\max(0, C_M\omega_k)(v_{k+1} - v_k) - \frac{h_k}{a}\sum_{j=1}^{n}G_{kj}\frac{\partial(h_j - H_j)}{\partial\theta}$$

$$+(\tau_{\theta_{k-1}} - \tau_{\theta_k})/\rho_0 + \frac{A}{a^2\cos^2\theta}\left[\frac{\partial(h_k e_{\phi\theta_k}\cos\theta)}{\partial\phi} + \frac{\partial(h_k e_{\theta\theta_k}\cos^2\theta)}{\partial\theta}\right] \qquad (2)$$

$$\frac{\partial h_k}{\partial t} + \nabla\cdot\vec{V}_k = \omega_k - \omega_{k-1} - \hat{K}_4\nabla^2(\nabla^2(h_k - H_k)) \qquad (3)$$

where

$$\nabla\cdot\vec{F} = \frac{1}{a\cos\theta}\frac{\partial F_\phi}{\partial\phi} + \frac{1}{a\cos\theta}\frac{\partial(F_\theta\cos\theta)}{\partial\theta};$$

$$\nabla^2\Phi = \frac{1}{a^2\cos^2\theta}\frac{\partial^2\Phi}{\partial\phi^2} + \frac{1}{a^2\cos\theta}\frac{\partial}{\partial\theta}\left(\frac{\partial\Phi}{\partial\theta}\cos\theta\right);$$

A = coefficient of isopycnal eddy viscosity; a = radius of the Earth (6371 km); C_b = coefficient of bottom friction; C_k = coefficient of interfacial friction; C_M = coefficient of

additional interfacial friction associated with entrainment; $D(\phi,\theta) = $ total depth of the ocean at rest; $\vec{e}_k = $ angular deformation tensor;

$$e_{\phi\phi_k} = \frac{\partial}{\partial\phi}\left(\frac{u_k}{\cos\theta}\right) - \cos\theta\frac{\partial}{\partial\theta}\left(\frac{v_k}{\cos\theta}\right) = -e_{\theta\theta_k};$$

$$e_{\phi\theta_k} = \frac{\partial}{\partial\phi}\left(\frac{v_k}{\cos\theta}\right) + \cos\theta\frac{\partial}{\partial\theta}\left(\frac{u_k}{\cos\theta}\right) = e_{\theta\phi_k};$$

$G_{kj} = g$, $j \geq k$; $G_{kj} = g - g(\rho_k - \rho_j)/\rho_0$, $j < k$; $g = $ acceleration due to gravity (9.8 m s^{-2}); $H_k = k$th layer thickness at rest; $H_n = D(\phi,\theta) - \sum_{j=1}^{n-1} H_j$; $h_k = k$th layer thickness; $h_k^+ = k$th layer thickness at which entrainment starts; $h_k^- = k$th layer thickness at which detrainment starts; $\hat{K}_4 = $ coefficient of biharmonic horizontal layer thickness diffusivity; $t = $ time; $\vec{V}_k = h_k\vec{v}_k = \vec{e}_\phi U_k + \vec{e}_\theta V_k$; $\vec{v}_k = k$th layer velocity $= \vec{e}_\phi u_k + \vec{e}_\theta v_k$; $W_k(\phi,\theta) = k$th interface weighting factor for global dispycnal mixing designed to conserve mass within a layer in compensation for explicit diapycnal mixing due to $h_k < h_k^+$ (i.e. $\omega_k^+ - \omega_k^-$), and net transport through the lateral boundaries of layer k; $\overline{X(\phi,\theta)} = $ region wide area average of X; $\phi = $ longitude; $\theta = $ latitude; $\rho_0 = $ constant reference density; $\rho_k = k$th layer density, constant in space and time; $\vec{\tau}_w = $ wind stress;

$$\vec{\tau}_k = \begin{cases} \vec{\tau}_w & \text{for } k = 0 \\ C_k \rho_0 |\vec{v}_k - \vec{v}_{k+1}|(\vec{v}_k - \vec{v}_{k+1}) & \text{for } k = 1 \ldots n-1 \\ C_b \rho_0 |\vec{v}_n| \vec{v}_n & \text{for } k = n; \end{cases}$$

$\Omega = $ angular rotation rate of the Earth (7.292205 $\times$ 10^{-5} s^{-1});

$$\omega_k = \begin{cases} 0 & k = 0, n \\ \omega_k^+ - \omega_k^- - W_k \hat{\omega}_k & k = 1 \ldots n-1; \end{cases}$$

$\omega_k^+ = \tilde{\omega}_k [\max(0, h_k^+ - h_k)/h_k^+]^2$; $\omega_k^- = \tilde{\omega}_k [\max(0, h_k - h_k^-)/h_k^+]^2$; $\hat{\omega} = \overline{(\omega_k^+ - \omega_k^-)}/\overline{W}_k$; and $\tilde{\omega}_k = k$th interface reference diapycnal mixing velocity.

   The model boundary conditions are kinematic and no slip. Although the model can run in thermodynamic mode (Metzger et al., 1992; Heburn, 1994; Jacobs et al., 1994; Metzger and Hurlburt, 1996), the simulations used here are purely hydrodynamic. As a result, thermal forcing and steric anomalies due to heating and cooling are excluded. However, the model does permit diapycnal mixing (cross-interfacial mixing of mass and momentum, but not heat in hydrodynamic mode) and it does permit ventilation of the interfaces between the model layers (isopycnal outcropping). This capability is essential to allow cross-layer closed mean vertical circulations within the model domain and to permit shallow layers in a basin-scale model. In essence, when any layer $k < n$ becomes thinner than a chosen value (h_k^+), water from the layer below is entrained into it at a velocity (ω_k) needed to prevent nonpositive layer thickness. Detrainment from thick layers due to $h_k > h_k^-$ was deactivated by setting h_k^- to a large value. Mass and volume are conserved within each layer by requiring no net transfer of mass across each layer

interface. The net mass flux across interface k, due to (1) outcropping and/or (2) any net transport of mass into or out of the layer above via ports in the lateral model boundaries, is balanced by the domain integral of diapycnal mixing across layer interface k ($\iint W_k \overline{\omega}_k$). The weight function for this diapycnal mixing, W_k, is uniform in the subtropical Atlantic model. In the global model, W_k is nonuniform, except for the shallowest interface, and has both positive and negative values based on oxygen saturation, as discussed by Shriver and Hurlburt (1997). This allows broad, slow diapycnal upwelling over much of the world ocean interior in addition to regions of diapycnal downwelling.

A hydrodynamic reduced-gravity model with n active layers has the lowest layer infinitely deep and at rest, i.e. $\vec{v}_{n+1} = 0$, $h_{n+1} = \infty$, and $\nabla h_{n+1} = 0$. The model equations for the active layers are identical to those for an n layer hydrodynamic finite depth model, except that $H_n = \text{constant}$; $G_{kl} = g(\rho_{n+1} - \rho_k)/\rho_0$, $l \le k$; $G_{kl} = g(\rho_{n+1} - \rho_l)/\rho_0$, $l > k$; $\vec{\tau}_k = \vec{\tau}_w$, $\quad k = 0$; $\vec{\tau}_k = C_k \rho_0 |\vec{v}_k - \vec{v}_{k+1}| (\vec{v}_k - \vec{v}_{k+1})$, $\quad k = 1 \dots n$; $\omega_k = 0$, $k = 0$; $\omega_k = \max(0, \omega_k^+) - \max(0, \omega_k^-) - h_k \hat{\omega}_k$, $k = 1 \dots n$.

In this paper, a reduced gravity version of the model was used only for two linear simulations used for comparison to the results of the nonlinear simulations. For all of the simulations, the model equations were integrated on a C-grid (Mesinger and Arakawa, 1976, Chap. 4, p. 47) using second-order centered finite differences in space and, for most, a semi-implicit time scheme. In the semi-implicit scheme, the external gravity waves and a user chosen number of the internal gravity wave modes are treated implicitly in a manner patterned after Kwizak and Robert (1971). This approach allows a much longer time step than possible with an explicit PE free surface model and longer than possible in an explicit PE, rigid-lid model. The user may choose to treat some of the slower internal gravity modes explicitly to avoid the solution of the Helmholtz equation required for each mode treated semi-implicitly. For the modes treated explicitly, there is an option to increase the time step using a method described by Brown and Campana (1978).

The model handles realistic rough bottom topography like seamounts without serious numerical problems (Hurlburt and Thompson, 1980), but it is confined to the lowest layer. This allows a modal decomposition in the vertical, semi-implicit treatment of all the vertical modes, and the formation of a separable Helmholtz equation for each mode. A separable Helmholtz equation is especially advantageous for the external mode, where the Helmholtz term is small, because it allows solution by a fast direct method such as the direct capacitance matrix technique used here (Hockney, 1968, 1970). The resulting reduction in topographic amplitude has minimal effect on three of the main reasons for including bottom topography: abyssal flow following topographic f/h contours, regulation of baroclinic instability, and upper ocean—topographic coupling via baroclinic instability. The latter allows eddy-driven abyssal currents (and thus, the bottom topography) to steer upper ocean currents, which do not directly impinge on the topography. This includes their mean pathways (Hurlburt et al., 1996a,b; Hurlburt and Metzger, 1998). However, abyssal currents driven by any means can do this (Hurlburt and Thompson, 1980, 1982; Thompson and Schmitz, 1989). Flow through straits with shallow sills is constrained to small values below the still depth. When the layered model equations are cast in transport form as was done here, the continuity Eq. (2) is

linear and differentiation of the topography in a nonlinear term of the continuity equation is avoided. Instead, the topography appears in the pressure gradient term of the momentum Eq. (1) in a numerically benign multiplicative form. See Hurlburt and Thompson (1980), Wallcraft (1991), and Moore and Wallcraft (1998) for detailed discussions of the numerics.

3. Design of the model simulations

Information about the simulations used in this investigation can be found in Table 1 and additional model parameters in Table 2. We focus on the nonlinear $1/8°$, $1/16°$, $1/32°$, and $1/64°$ subtropical basin-scale Atlantic simulations which include the Caribbean and Gulf of Mexico and which use the same wind forcing. The nonlinear simulations include the associated impacts of, e.g. flow instabilities, bottom topography, isopycnal outcropping, vertical mixing and multiple vertical modes. The nonlinear simulations also include effects of the global thermohaline circulation via ports in the northern and southern model boundaries, including a southward DWBC and a northward upper ocean return flow. In this paper, we focus on assessing the impacts of model resolution on model–data comparisons. The model experiments are not designed to unravel dynamical impacts of various model features. That will be the subject of a second paper.

Several additional simulations are used, but only to help interpret the model–data comparison results of the core simulations. The linear simulations are included to demonstrate a well-understood baseline ocean model response to atmospheric forcing and to help assess and interpret the net impacts of the added capabilities of the nonlinear simulations and the changes in those impacts as the resolution is increased. The linear simulation means exclude not just nonlinearity, but all of the associated impacts listed above. Simulations forced by two different wind stress climatologies help in assessing the sensitivity of the model results to the choice of wind set forcing. The global simulations are used (1) to investigate the effects of 6 to 12 hourly interannual wind forcing on Gulf Stream system variability by comparison to variability obtained using monthly climatological forcing and (2) to help assess the impact of the subtropical Atlantic model boundaries at 9°N and 47°N or 51°N. The Atlantic model is designed to be a basin-scale model which encompasses the North Atlantic subtropical gyre, including its extensions into the Caribbean and Gulf of Mexico, and is thus appropriate to study the Gulf Stream system in a basin-scale context.

Because the model layers are Lagrangian in the vertical (varying in thickness and depth with both space and time) and they are based on a physical approximation (integration of the equations through a layer), rather than on a finite difference approximation as used in models with fixed levels in the vertical, good simulations can be obtained using relatively few layers compared to the number of levels needed for fixed level models. With the layered ocean model design, experience has shown that increasing the horizontal resolution generally has a much greater impact on the realism of model circulation features than increases in vertical resolution (Hurlburt et al., 1996b). Hence, we focus on horizontal resolution increases in this paper. In addition, the model–data comparisons provide feedback on the adequacy of the model design.

Table 1
Atlantic and global simulations with $1/8°$ to $1/64°$ resolution

Simulation[a]	Resolution[b]			Model domain[c]	A^d (m^2 s^{-1})	Wind forcing[a]	Years spanned[e]	Comments
	Latitude	Longitude	# Layers					
8H	1/8°	45/256°	5	Atlantic 9°N–47°N	100	HR	106–125	All Atlantic simulations include the Caribbean and Gulf of Mexico
16H	1/16°	45/512°	5	Atlantic 9°N–47°N	20	HR	55–66	
16LH	1/16°	45/512°	1.5	Atlantic 30°S–65°N	30	HR	152–180	Linear reduced gravity
16LC	1/16°	45/512°	1.5	Atlantic 30°S–65°N	30	COADS	131–153	Linear reduced gravity
16GH	1/16°	45/512°	6	Global 72°S–65°N	20	HR	847–910	
16GI	1/16°	45/512°	6	Global 72°S–65°N	20	ECMWF/HR	1979–1997	6–12 hourly interannual hybrid wind forcing
32H	1/32°	45/1024°	5	Atlantic 9°N–47°N	10	HR	84–98	
32C	1/32°	45/1024°	5	Atlantic 9°N–51°N	7	COADS	56–75	
64H	1/64°	45/2048°	5	Atlantic 9°N–51°N	3	HR	62–75	

In general, the model simulations were spun up from rest at progressively higher resolution until they were close to statistical equilibrium at each resolution. The same forcing functions (winds and port transport values) were used at each resolution to minimize additional large-scale spin up due to the resolution change. Three different wind sets were used in driving simulations for this study, two monthly climatologies and an interannual wind set with 6 to 12 hourly temporal resolution. The Hellerman and Rosenstein (1983) (HR) monthly wind stress climatology was the primary wind forcing. It is based on ship winds collected from 1870 to 1976 and is provided on a 2° grid. It was smoothed with one pass of a nine-point real smoother to eliminate two-grid interval noise. This noise is not seen when wind stress curl is calculated using centered differences on the 2° grid, but is very apparent when HR is interpolated to the finer ocean model grids and the curl is then calculated. The comprehensive ocean–atmosphere data set (COADS) (Woodruff et al., 1987) is the source of the other monthly wind stress climatology used to force the model. COADS data from 1945 to 1989 were analyzed on a 1° grid by da Silva et al. (1994a,b). The HR and COADS analyses were performed without assimilation by a numerical atmospheric model. See Townsend et al. (2000, this issue) for additional discussion of these monthly wind stress climatologies and nine others used in a comparison of linear ocean model response to the different wind sets.

Notes to Table 1:

[a] The simulation naming convention follows. The number corresponds to the grid resolution. C, H, and I refer to COADS (the official DAMEE-NAB wind set), Hellerman and Rosenstein (1983) (HR) and interannual wind forcing, respectively, where I refers to ECMWF/HR hybrid 6–12 hourly interannual wind forcing with the 1979–1993 mean from the ECMWF reanalysis replaced by the HR annual mean. L refers to 1.5-layer linear reduced gravity simulations with an active upper layer and a lower layer that is infinitely deep and at rest. G refers to simulations with a nearly global domain; the rest are Atlantic simulations. As discussed at the beginning of Section 5, HR was chosen for the core simulations rather than COADS.

[b] Resolution for each prognostic variable. The convention for reduced gravity simulations is to call the inert bottom layer half a layer.

[c] With a few exceptions, like the Gulf of Mexico, the 200 m isobath near the shelf break is used as the model boundary. The topographic amplitude with respect to 6500-m depth (the maximum depth allowed) is multiplied by 0.82 in the finite depth Atlantic simulations and 0.69 in the global simulations to confine it to the lowest layer. Flow through shallow straits is constrained to small values below the sill depth. Originally, 47°N was chosen the most geometrically and dynamically natural location for the northern boundary of the subtropical Atlantic domain. Later, it was moved to 51° to reduce the tendency for an unrealistic eastward current to form along the northern boundary (because 47°N is south of the subtropical gyre northern boundary) and to reduce the associated numerical problems near the outflow port. It was also done to separate natural variability east of the Grand Banks from variability associated with the outflow port and any unrealistic northern boundary current. As shown in Section 6.5, this was clearly beneficial for the 1/64° model. However, to best show the impact of increasing resolution, the overall most realistic HR-forced simulation we had at each resolution was used here, and thus, some with a boundary at 47°N were chosen.

[d] A is the coefficient of isopycnal eddy viscosity, Eqs. (1) and (2).

[e] The simulations were initialized from a simulation of compatible design already spun-up to statistical equilibrium at the same or coarser resolution to minimize additional large-scale spin-up. Except for the interannual simulation, which lists calendar years, the years preceding the model ''years spanned'' by each simulation were covered by parent simulations(s) with year 1 starting from rest. Using a thick abyssal layer greatly reduced the spin-up time required by removing the need for deep diapycnal diffusion in the model.

Table 2
Additional model parameters

Simulation group	Mean layer depths $[\Sigma_{i=1}^{k} H_i \text{ (in m)}]$	Stratification[a] $[\rho_{k+1} - \rho_k \text{ (in kg m}^{-3})]$	Port transports for each layer in Sv[b]		h_k^+ (in m)	$\tilde{\omega}_k$ (in cm s^{-1})
			Northern boundary	Southern boundary		
Nonlinear Atlantic	250/500/750/ 1000/bottom	1.01/0.40/0.31/0.41	6.5/4.84/2.33/ 0.33/ − 14	6.5/4.5/2.0/ 0.0/ − 13	50/40/40/40	0.07
Linear Atlantic	250/∞	1.76	0	0	N/A[c]	N/A
Global	155/340/600/ 975/1500/bottom	1.34/0.44/0.27/ 0.23/0.24	3.5/3.5/2.8/ 2.1/2.1/ − 14	No ports	50/40/40/40/40	0.05

Other model parameters

Parameter	Definition	Value
C_b	Bottom friction coefficient	0.002 (N/A in the linear simulations)
C_k	Interfacial stress coefficient	0
C_M	Coefficient of additional interfacial friction associated with entrainment	1 (N/A in the linear simulations)
g	Acceleration due to gravity	9.8 m s^{-2}
ρ_o	Reference density	1000 kg m^{-3}
$\hat{K}_4$	Coefficient of biharmonic layer thickness diffusivity	0

[a] Stratification is derived using domain averages from Levitus (1982) and the mean interface depths from an earlier spun-up simulation with a similar model domain and layer structure.

[b] The ports are designed to include the global thermohaline component of the Atlantic circulation based on observational knowledge (see text). The Atlantic model ports are confined to western segments of the northern and southern boundaries. The port transports in the nearly global model are sums over four ports: Davis Strait, Denmark Strait, Iceland to Faroes Islands, and Faroes to Shetland Islands (see Shriver and Hurlburt, 1998). Transports are positive northward and eastward, negative southward and westward. 1 Sv = 10^6 m^{3}s^{-1}.

[c] N/A = not applicable.

The interannual forcing was derived from the six hourly European Centre for Medium-range Weather Forecasts (ECMWF) reanalysis which covers 1979–1993 and from 12 hourly ECMWF archived operational analyses over 1994–1997. The ECMWF analyses were performed by assimilation into the ECMWF global numerical atmospheric spectral model with T106 resolution (1.7° along the equator) for the reanalysis and T213 resolution (0.85° along the equator) for the archived operational analyses (ECMWF, 1994, 1995; Gibson et al., 1996, 1997). The reanalysis has the advantages that, unlike archived operational products, the atmospheric model and the data assimilation techniques were not changed over the time frame of the analysis and data not available by the operational cutoff time were included. The 1000-mb analyses we used had been spectrally truncated and were provided on a 2.5° grid. The ECMWF 1000-mb winds were chosen over the ECMWF 10 m winds or surface stresses because the reanalysis and operational winds are more consistent at 1000 mb than 10 m, based on time series of variance over the ocean averaged from 40°S to 40°N. The 1000-mb winds were adjusted for spatial variations in the height of the 1000-mb surface by E.J. Metzger (personal communication) and the winds were converted to surface stresses using a constant drag coefficient of $C_D = 1.5 \times 10^{-3}$ and air density $\rho_{air} = 1.2$ kg m^{-3}. To form the ECMWF/HR hybrid winds used to force simulation 16GI (Table 1), the temporal mean over 1979–1993 from the ECMWF reanalysis was subtracted from each analysis in the interannual time series used to force the ocean model, and replaced by the annual mean from HR. The amplitude of the wind stress seasonal cycle is about the same for the HR monthly climatology and a monthly climatology calculated from the ECMWF stresses discussed above (again averaged over the ocean from 40°S to 40°N).

A significantly modified version of the 1/12° ETOP05 bottom topography (NOAA, 1986) was used in the 1/8°, 1/16°, and 1/32° simulations. The ETOP05 topography was first interpolated to the 1/16° model grid, then modified for better agreement with detailed bathymetric charts (McManus et al., 1997). Mostly, the location of the 200-m isobath, used as the model boundary in most locations, was modified for better agreement with the bathymetric charts. The 1/8° and 1/32° model boundaries were formed by interpolation from the 1/16° model grid with subsequent minor modification.

The 1/64° model geometry and bottom topography (Fig. 1) were formed in a careful, thorough process similar to that used to define the 1/16° topography, except that the 1/24° DAMÉE-NAB project North Atlantic topography developed by Ziv Sirkes, Department of Marine Sciences, University of Southern Mississippi (personal communication) was used as the starting point. This topography is a descendent of ETOP05, but with substantial improvement, first by GEOPHYSICAL EXPLORATION TECHNOL-OGY (GETECH, Dept. of Earth Sciences, University of Leeds) who created a 1/12° global Digital Terrain Model (DTM5) and a 1/24° European region (25°W–60°E; 30°N–85°N) DTM25. The 1/24° DAMÉE topography covers the region 0°–75°N, 98°W–42°E and was formed by (a) interpolating DTM5 to 1/24°, then merging it with DTM25 and National Ocean Service data for the US coastal region. It was further modified using 0, 20, 100, and 1000 m isobaths digitized from bathymetric charts and point measurements around the Caribbean Islands and the South and North American coasts (Z. Sirkes, personal communication). In the Gulf of Mexico, the model geometry uses 50 to 100 m isobaths as the model boundary because the Loop Current in the Gulf
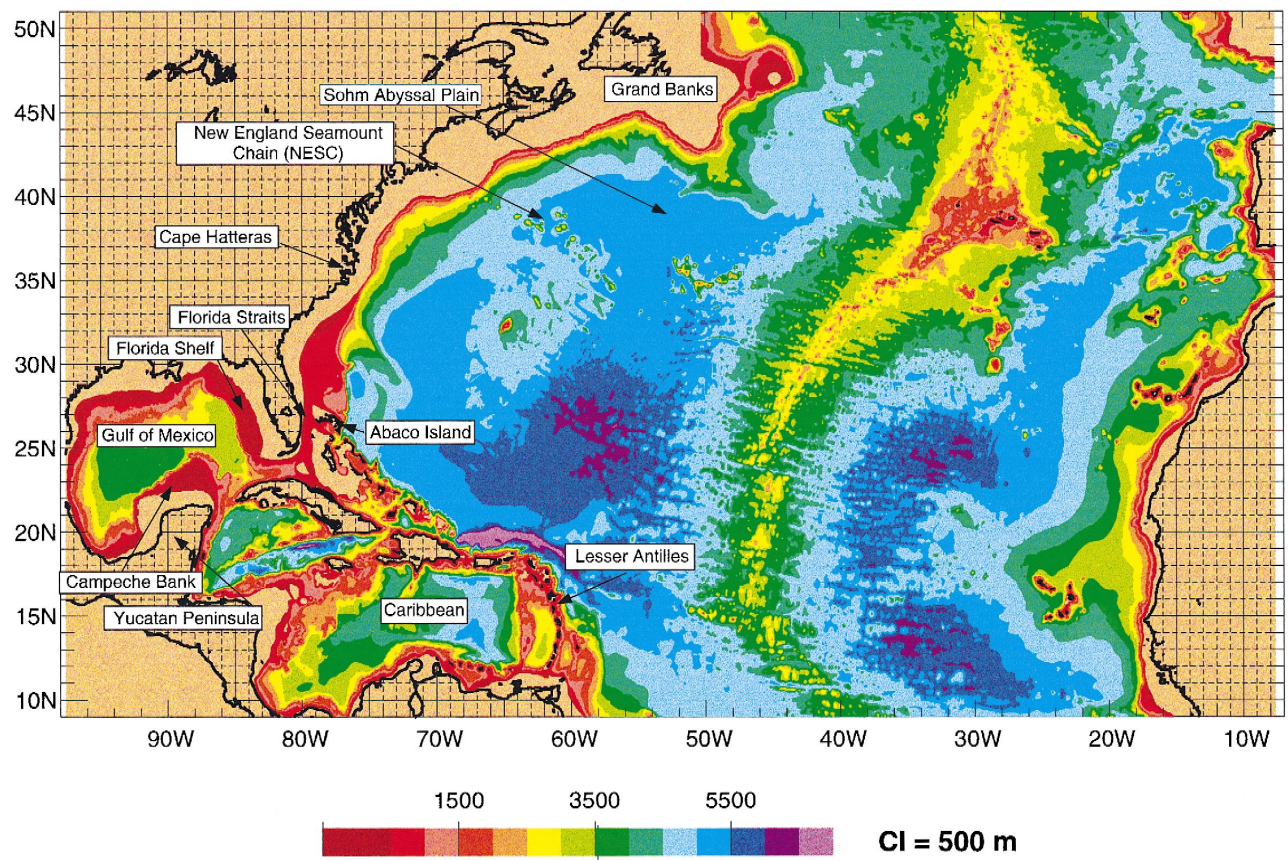
Fig. 1. A 1/64° subtropical Atlantic model domain and bottom topography. In most locations, the model boundary is at the 200 m isobath. The contour interval is 500 m.

of Mexico can intrude to depths shallower than 200 m over the southwest Florida Shelf and the Campeche Bank north of the Yucatan Peninsula. It is necessary to avoid having the model geometry reduce the width of the neck of the Loop Current between the Campeche Bank and the Florida Shelf to less than observed because that can cause a port separation β Rossby number high enough to prevent the observed eddy shedding by the Loop Current in the Gulf of Mexico (Hurlburt and Thompson, 1980, 1982). Finally, the topographic depths were smoothed twice using a nine-point real smoother to reduce energy generation at small scales that are poorly resolved by the model.

The global thermohaline contribution to the Gulf Stream system is included via ports in the western portion of the northern and southern boundaries of the subtropical Atlantic model and in the northern boundary of the global model. Above the abyssal layer, the net transport is northward and contributes to the Gulf Stream. In the abyssal layer, the net transport is southward mainly in the form of a DWBC. The location, amplitude, and depth profile of the specified port flows were chosen based on observational knowledge (e.g. Schmitz and Richardson, 1991; Mauritzen, 1993; Schmitz and McCartney, 1993; Fratantoni et al., 1995; Fratantoni, 1996; Schmitz, 1996) in consultation with W. Schmitz, D. Fratantoni and W. Johns (personal communication). In the subtropical Atlantic model, the net transport through the northern (southern boundary) is 14 Sv (13 Sv) northward above the abyssal layer and 14 Sv (13 Sv) southward as a DWBC in the abyssal layer (Table 2). This gives a net upward transport of 1 Sv from the abyssal layer to layers above within the model domain with uniform distribution of this upward transport. In the global model, the three eastern ports in the northern North Atlantic (Denmark Strait, Iceland-Faroes, and Faroes-Shetland) carry 12 Sv northward (southward) above (in) the abyssal layer. They are designed to include the effects of deep water formation outside the model domain plus the augmentation of North Atlantic deep water formation by entrainment as the southward overflow from the sills sinks to deeper depths (Mauritzen, 1993; Schmitz, 1996). The 2 Sv northward (southward) above (in) the abyssal layer through the port at the Davis Strait are designed to augment the effects of deep water formation in the Labrador Sea, which was only about 1 Sv from the oxygen-based diapycnal mixing scheme discussed in Section 2 and in more detail by Shriver and Hurlburt (1997). See Shriver and Hurlburt (1998) for more details on the design of the global model ports.

Earlier versions of NLOM have been used in numerous Gulf Stream modeling studies which investigated model–data comparisons, Gulf Stream separation at Cape Hatteras, the effects of the DWBC on Gulf Stream separation, resolution requirements for Gulf Stream modeling, data assimilation and Gulf Stream forecasting, distribution and amplitude of mesoscale variability in comparison to observations, and the impact of the New England Seamount Chain (NESC) on the mean path and variability of the Gulf Stream (Hurlburt and Thompson, 1984; Thompson and Schmitz, 1989; Hallock et al., 1989, 1991; Thompson et al., 1992; Fox et al., 1992, 1993; Schmitz and Thompson, 1993; Smedstad and Fox, 1994; Spall, 1996a,b; Gallacher and Hogan, 1998). Except for Thompson et al. (1992) and Gallacher and Hogan (1998), these used sub-basin scale models designed to focus on the Gulf Stream region between Cape Hatteras and the Grand Banks or the Florida Straits and the Grand Banks. In addition, there is a companion article in this issue (Townsend et al., 2000) which uses NLOM to investigate

linear Atlantic model responses to 11 different monthly wind stress climatologies. NLOM has also been used to investigate ocean dynamics, resolution requirements, model–data comparisons, data assimilation and observing system simulation related to the Kuroshio, the corresponding western boundary current in the Pacific (Hogan et al., 1992; Hurlburt et al., 1992, 1996a,b; Jacobs et al., 1994, 1996; Carnes et al., 1996; Mitchell et al., 1996; Smedstad et al., 1997; Hurlburt and Metzger, 1998). Most of these used an eddy-resolving basin-scale Pacific model north of 20°S, but regional versions and a global model were also used.

4. Comparison of $1/16°$ linear and $1/32°$ nonlinear simulations forced by two different wind sets

We start by investigating the extent to which nonlinearity and associated effects (beginning of Section 3) are required to obtain realistic simulations of the Gulf Stream region and the sensitivity of the linear and nonlinear simulations to the wind set used to force the model. Here, we compare results from a $1/16°$ linear 1.5 layer reduced gravity model and a $1/32°$ nonlinear five-layer model with realistic bottom topography. Each model was forced by two different monthly wind stress climatologies, Hellerman and Rosenstein (1983) (HR) (simulations 16LH and 32H, Table 1) and COADS (simulations 16LC and 32C). These simulations were spun up to statistical equilibrium as described in Section 3.

Fig. 2 shows the mean SSH from the two linear simulations. An observed mean Gulf Stream axis determined from TOPEX/Poseidon satellite altimetry (Lee et al., 1997) is superimposed on each SSH mean. Dynamically, these linear simulations are essentially the same as Munk (1950) with a Sverdrup (1947) interior calculated using realistic wind forcing and model boundaries, including islands. Both linear simulations show two unrealistic mean Gulf Stream pathways in the region between Cape Hatteras and the Grand Banks, one proceeding due east from Cape Hatteras and a second one continuing northward along the western boundary until forced eastward by the regional northern boundary. Townsend et al. (2000, this issue) discuss the reason for the two pathways in the linear simulations. They also show that the northern pathway is augmented when a linear version of the upper ocean global thermohaline contribution to the Gulf Stream is included as a Munk (1950) western boundary layer driven via open ports in the northern and southern boundaries of the model domain. Obviously, a major change is required to get from the two unrealistic linear Gulf Stream pathways to a realistic nonlinear pathway between Cape Hatteras and the Grand Banks.

The shape of the subtropical gyre is a striking difference between the two linear simulations, a pronounced C-shape with COADS forcing and the absence of a C-shape with HR forcing. Again, the reason for this is discussed by Townsend et al. (2000, this issue). The difference is so pronounced that the maximum western boundary current transport at 30°–31°N in the subtropical gyre driven by HR is the location of a minimum with COADS forcing. However, the Florida Straits transport at 27°N and the western boundary current transport at 34°N, just south of where the Gulf Stream separates from the coast at Cape Hatteras, are in much better agreement in the two linear simulations, as
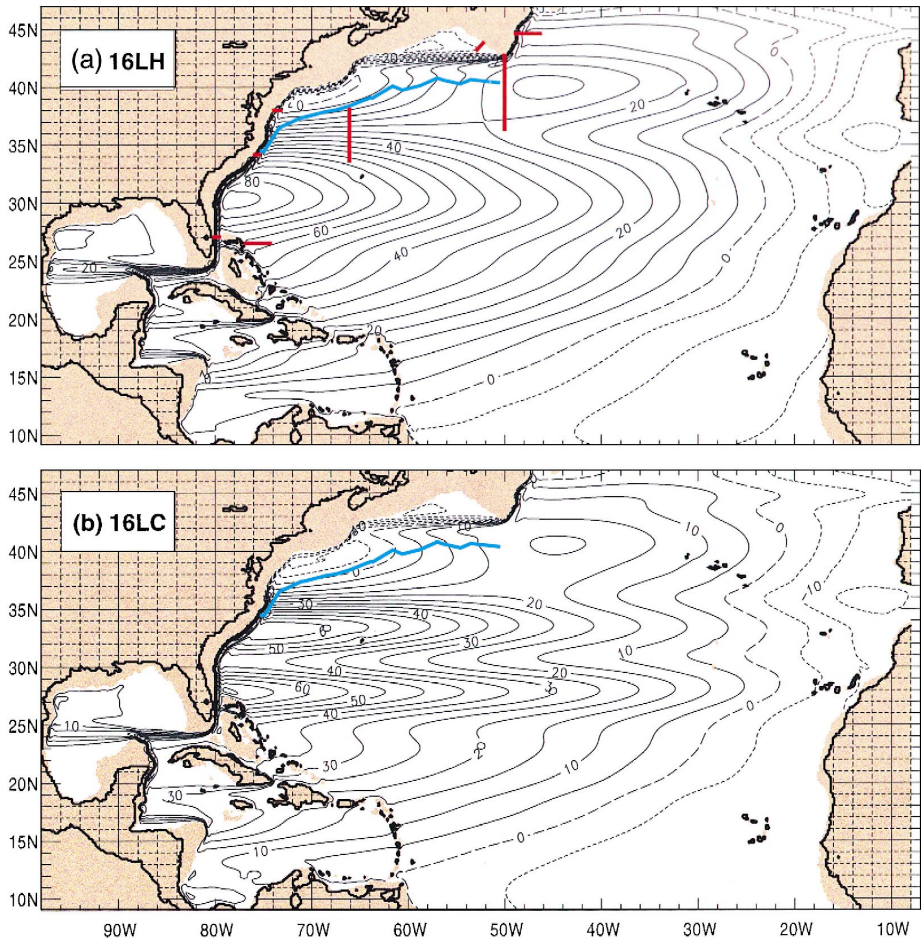
Fig. 2. Whole domain mean sea surface height (SSH) from two 1/16°, 1.5-layer linear reduced-gravity simulations. (a) Simulation 16LH (Table 1) forced by the Hellerman and Rosenstein (1983) monthly wind stress climatology, and (b) simulation 16LC forced by the COADS (da Silva et al., 1994a,b) monthly wind stress climatology. The mean axis of the Gulf Stream from TOPEX/Poseidon altimetry (Lee et al., 1997) is superimposed. The contour interval is 5 cm. Selected transport sections are marked on (a). The section marked for the Gulf Stream at 68°W is the section used for linear simulation 16LH. The N–S limits of this section were adjusted for each simulation to capture the modeled Gulf Stream transport at 68°W.

shown in Table 3. Furthermore, when a 13 Sv contribution from the upper ocean branch of the global thermohaline circulation is added and the total western boundary current transport at 27°N above the abyssal layer is compared (''sum of above'' in Table 3), the linear and nonlinear simulations all agree within 10% of the well-observed value from Larsen (1992) and Lee et al. (1996). In contrast, the observed and nonlinear simulation Gulf Stream transports at Cape Hatteras are much higher than the linear simulation transports with the global thermohaline contribution added.

Table 3
Mean Gulf Stream transports in Sv, simulated vs. observed at selected locations
Sections marked on Fig. 2. Transports exclude the abyssal layer.

	Simulated						Observed[a]
	16LH	16LH+T[b]	16LC	16LC+T[b]	32H	32C	
Florida Straits at 27°N	26	39	24	37	36	28	32
East of Abaco Island at 26.5°N	−1	−1	0	0	3	6	5
Sum of above[c]	25	38	24	37	39	34	37
Gulf Stream at Cape Hatteras	26	39	24	37	64	56	63

[a] Observed values were obtained from Richardson and Knauss (1971), Larsen (1992), Lee et al. (1996), and Schmitz (1996).

[b] +T means a 13 Sv contribution from the upper ocean branch of the global thermohaline circulation (Schmitz and Richardson, 1991) was added to the western boundary current transport of the linear simulation. That contribution is already present in the nonlinear simulations.

[c] Measure of total upper ocean western boundary current transport at 27°N.

Between the Florida Straits and Cape Hatteras, nonlinearity and associated effects (Section 3) have gained a much more important role and both nonlinear simulations (Fig. 3) show a much more realistic Gulf Stream pathway between Cape Hatteras and the Grand Banks than the linear simulations (Fig. 2). This includes the observed Gulf Stream separation from the coast at Cape Hatteras. Overall, the HR and COADS forced nonlinear simulations show similar Gulf Stream pathways and similar large nonlinear recirculation gyres on the south side of the Gulf Stream. The latter augment the Gulf Stream transport, including the transport at Cape Hatteras. The two nonlinear simulations also show similar eastward penetration of the nonlinear recirculation gyre and a distinct eastern gyre in addition to the western one. The striking difference in the large-scale shape of the subtropical gyre seen in the linear simulations with HR and COADS is gone in the nonlinear simulations. The two nonlinear simulations show a similar C-shape in the subtropical gyre. This shape is different from that found in either linear simulation and it is a consequence of the large nonlinear recirculation gyre on the south side of the Gulf Stream, not the wind forcing.

5. Impact of resolution on nonlinear subtropical Atlantic simulations

In Section 4, we established that a $1/32°$ nonlinear basin-scale model can simulate a much more realistic Gulf Stream pathway between Cape Hatteras and the Grand Banks than a linear model forced by the same wind stress climatology. In this section, we begin to investigate the impact of model resolution on nonlinear, basin-scale simulations of the subtropical Atlantic. At each resolution, we want to avoid uncertainty about the relative roles of (a) the added capabilities of the nonlinear simulations and (b) Sverdrup flow due to wind stress curl in forming a subtropical gyre with a large scale C-shape. Thus, we focus on simulations forced by the HR wind stress climatology, which does not give a C-shape in linear simulations (Fig. 2), rather than use COADS, the official wind set for DAMÉE-NAB.
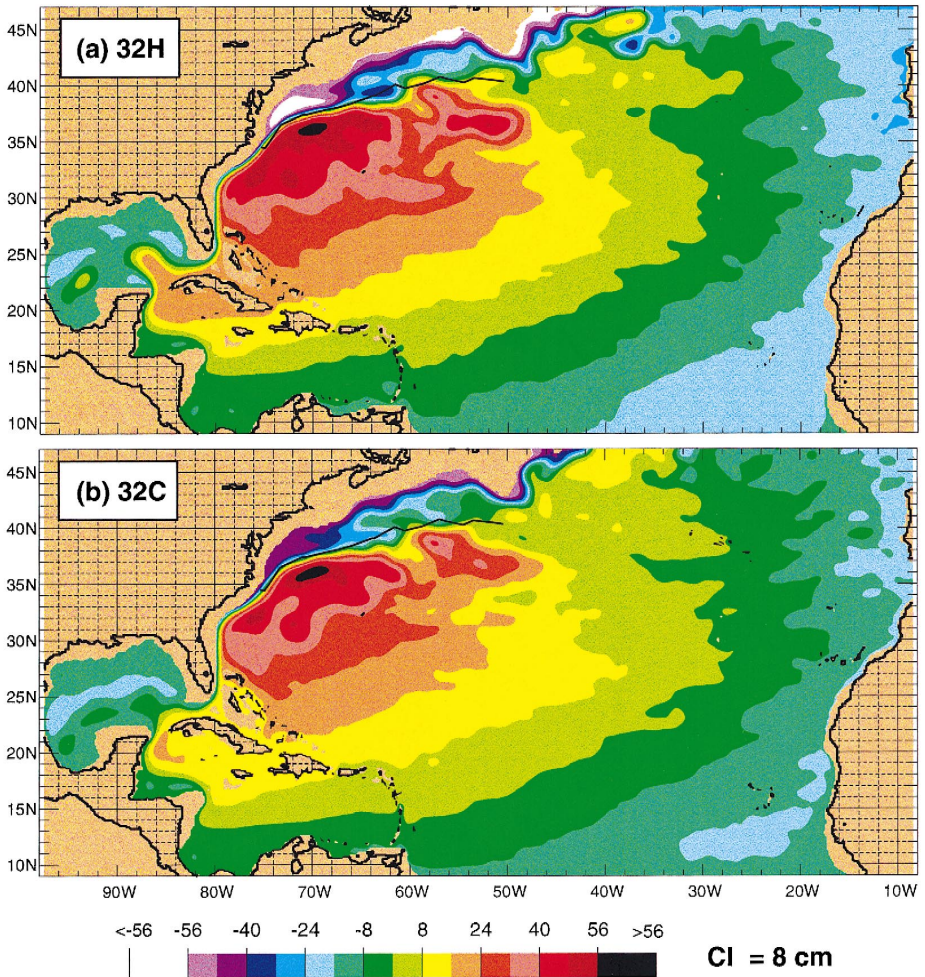
Fig. 3. Whole domain mean SSH from (a) a 1/32°, five-layer simulation with realistic bottom topography forced by the HR monthly wind stress climatology, simulation 32H in Table 1; (b) a simulation with essentially the same design, except forced by the COADS monthly wind stress climatology, simulation 32C in Table 1. In both, the global thermohaline circulation is included via ports in the northern and southern model boundaries (Table 2). The contour interval is 8 cm. The mean Gulf Stream axis from TOPEX/Poseidon altimetry (Lee et al., 1997) is superimposed.

In addition to the linear dynamics and nonlinearity, the nonlinear simulations add more layers, the barotropic mode, bottom topography, the DWBC, diapycnal mixing and the possibility of isopycnal outcropping. Dynamically, they add more vertical structure to the circulation (including an abyssal circulation which can be very different from the upper ocean circulation) and the potential for meridional overturning, inertial jets, flow instabilities, eddy-driven abyssal flows (Holland and Lin, 1975; Rhines and Holland, 1979), topographic steering of abyssal currents, steering of upper ocean currents by

abyssal currents driven by any means (Hurlburt and Thompson, 1980, 1982, 1984), such as the DWBC (Thompson and Schmitz, 1989) or flow instabilities (upper ocean—topographic coupling via a mixed baroclinic–barotropic instability (Hurlburt et al., 1996b; Hurlburt and Metzger, 1998)).

In this paper, we investigate the impact of model resolution on model–data comparisons using our overall best simulations at each resolution. Gulf Stream system dynamics will be the focus of a second paper. We already know from Fig. 3 that the model capabilities and dynamics just outlined are sufficient to produce realistic Gulf Stream separation at Cape Hatteras and a realistic Gulf Stream pathway between Cape Hatteras and the Grand Banks. How much resolution is needed to adequately represent the added
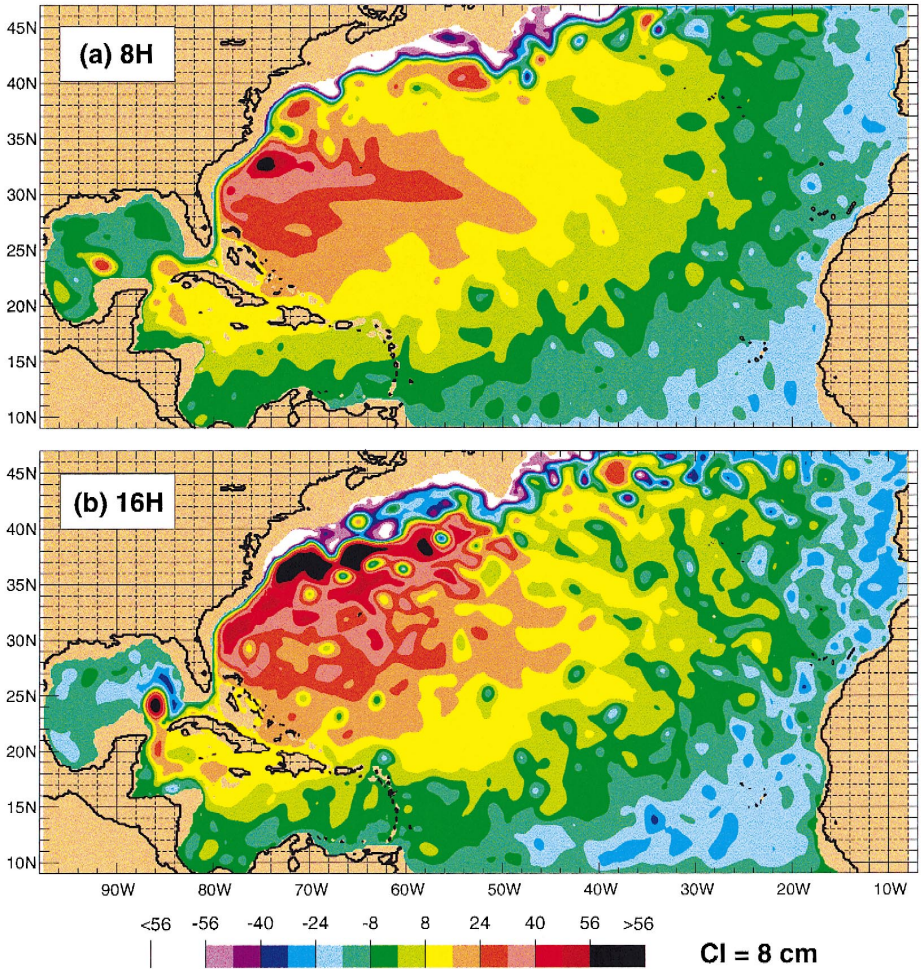
Fig. 4. Whole domain snapshots of SSH from five-layer simulations forced by the HR monthly wind stress climatology and the global thermohaline circulation with horizontal grid resolution of (a) $1/8°$ (simulation 8H), (b) $1/16°$ (simulation 16H), (c) $1/32°$ (simulation 32H), and (d) $1/64°$ (simulation 64H). See Table 1. The contour interval is 8 cm.
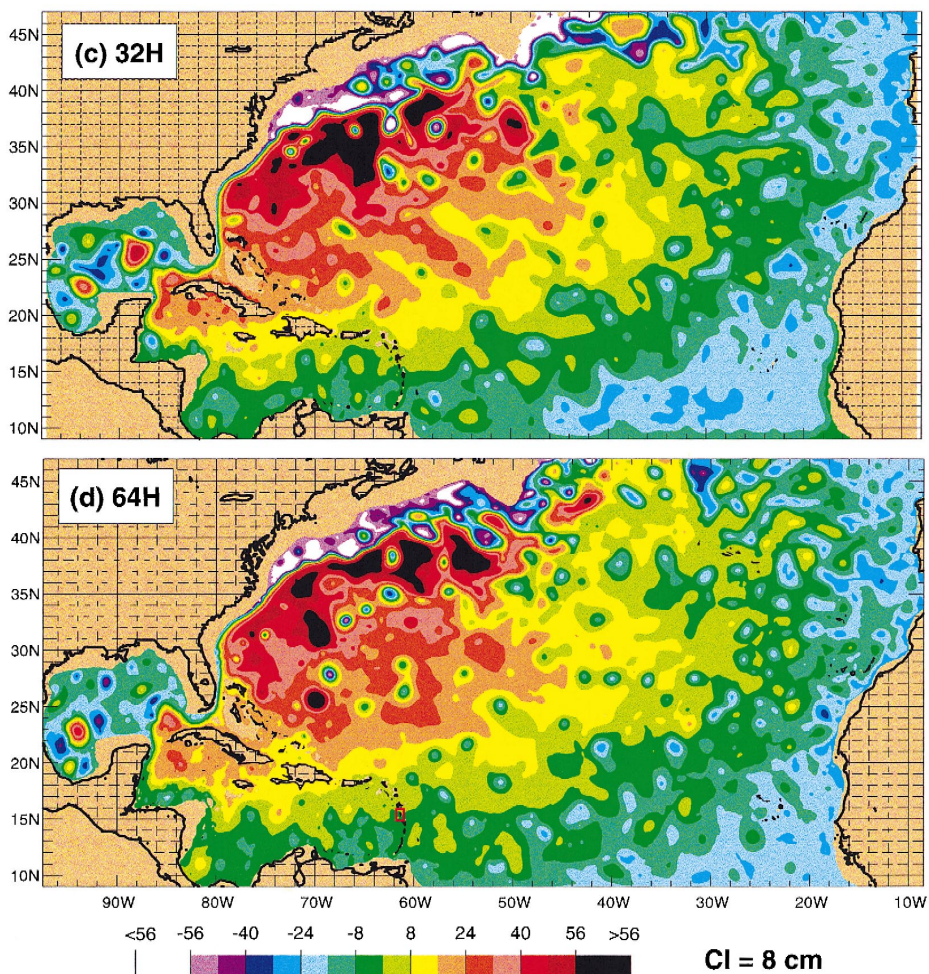
Fig. 4 (*continued*).

dynamics of the nonlinear simulations and obtain a realistic simulation of the Gulf Stream pathway, the large-scale shape of the subtropical gyre, the mesoscale eddy field, the abyssal circulation current transports and pathways, observed levels of variability in the upper ocean and the abyssal circulation and other aspects of the circulation? How do the simulations change as the resolution is increased and the eddy viscosity is reduced (as permitted by the resolution increases)? As the resolution is increased, do we see evidence of simulation convergence for mesoscale (~ 100 km) statistical properties and for larger scale circulation features? How do resolution requirements for realistic results vary from region to region and for different aspects of the circulation in the context of model–data comparisons? These are the main issues addressed in the remainder of this paper.

Some of the answers are indicated in snapshots of SSH from the nonlinear model at four different resolutions, 1/8° (14 km), 1/16° (7 km), 1/32° (3.5 km), and 1/64° (1.8 km) (Fig. 4). Quantitative model–data comparisons for means and variabilities are discussed in Section 6. The 1/8° simulation (Fig. 4a) basically shows a wiggly version of the two linear simulation Gulf Stream pathways (Fig. 2a) with the northern branch dominant because of the additional 13–14 Sv contribution from the thermohaline circulation in the nonlinear simulation. Realistic Gulf Stream separation at Cape Hatteras and a realistic Gulf Stream pathway between Cape Hatteras and the Grand Banks has been obtained for a limited period of time in a few 1/8° simulations driven by HR wind stresses, e.g. Thompson et al. (1992), but not as a robust feature.

Fig. 2 indicates that the smoothed HR wind stresses provide little assistance to the model in forming an eastward inertial jet from Cape Hatteras. The COADS wind forcing provides better assistance near Cape Hatteras but not in forming a continuous Gulf Stream pathway between Cape Hatteras and the Grand Banks. The ECMWF wind products are better for that, especially the 1983–1986 ECMWF 1000-mb winds used by Chao et al. (1996) (Townsend et al., 2000). However, as with the C-shape of the subtropical gyre, we want to avoid uncertainty about the relative roles of (a) the added capabilities of the nonlinear simulations and (b) Sverdrup flow in generating a realistic Gulf Stream pathway. Again, the smoothed HR wind stresses are a suitable choice to avoid an ambiguity and they do provide realistic western boundary current transport near latitude 27°N (Table 3).

At 1/16° resolution, we have experienced mixed success with Gulf Stream separation at Cape Hatteras and the Gulf Stream pathway between Cape Hatteras and the Grand Banks, but unlike the linear and 1/8° nonlinear simulations, only one Gulf Stream pathway is simulated in the region just east of Cape Hatteras as observed. Overall, simulation 16H (Table 1, Fig. 4b) is our most realistic 1/16° simulation of the Gulf Stream so far. In some simulations, we obtained realistic, robust Gulf Stream separation, in others Gulf Stream separation but with the pathway too far north just east of Cape Hatteras and in some, the pathway was similar to that of the dominant northern branch of the 1/8° simulation. This variation in the results was obtained using the standard smoothed HR wind stress forcing and 13–14 Sv thermohaline contribution (meridional overturning circulation), but with changes in other model parameters. Increasing the strength of the Gulf Stream by increasing the strength of the wind stress or the meridional overturning cell facilitated Gulf Stream separation at 1/16° resolution, but that was not essential and was not done in the simulation results shown here. E. Chassignet (personal communication) had a similar experience in association with the strength of the meridional overturning at this resolution, and, in general, similar experiences at this resolution (Table 4).

At 1/32° and 1/64° resolutions, Gulf Stream separation at Cape Hatteras is very robust and significant overshoot of the observed separation latitude, common at lower resolution, has not been a problem. East of the NESC, the nonlinear recirculation gyre is stronger than at 1/16° resolution and it penetrates farther to the east (Fig. 4). The size and strength of the nonlinear recirculation gyres at 1/32° and 1/64° resolutions has a profound effect on the large-scale shape of the subtropical gyre by creating a large-scale C-shape (Fig. 3, 4d) seen in weaker form in the 1/16° simulation (Fig. 4b), but not in

Table 4
Various definitions of grid resolution

Group	Definition of grid distance	Value for approximately the same resolution	Latitude where occurs
(1) Bleck/Chassignet ''square grid''[a]	Distance between like variables at equator (all grids)	1/12°	Equator
(2) NRL[b]	Distance between like variables (all grids)	1/16°	Uniform in latitude, square at 45°N
(3) Semtner/Chervin, Los Alamos ''square grid''[c]	Average distance between like variables 0° to extreme model latitude (all grids)	1/20°	53°N
(4) O'Brien[d]	Distance between unlike variables (C-grid)	1/32°	Uniform

[a] Bleck/Chassignet 1/12° grid is $45/512° \simeq 0.088° \simeq 1/12°$ in latitude×longitude at the equator. Square grid is $45/512°$ cos(latitude)×$45/512°$, latitude×longitude (Bleck et al., 1992; E. Chassignet, personal communication).

[b] NRL 1/16° grid is $1/16° \times 45/512°$ (latitude×longitude), which is ''square'' at 45°N.

[c] A distance weighted average of the latitudinal grid increments from the equator to the extreme latitude of the model is used in describing the resolution of the Semtner/Chervin and Los Alamos ocean models (McClean et al., 1997). For example, the 1/6° Alamos model has this resolution at 53° latitude, increasing from 0.28° resolution at the equator.

[d] Luther and O'Brien (1985).

the HR-driven linear simulation (Fig. 2a). At 1/8°, there is a C-shape farther north between the two unrealistic branches of the simulated Gulf Stream created by a narrow nonlinear recirculation gyre along the southern side of the northern branch.

Fig. 5 illustrates the meaning of 1/64° (1.8 km) resolution by showing a blow-up of a 1° square, marked by a red box on Fig. 4d. This box surrounds the island of Dominica, a medium-sized member of the Lesser Antilles island chain. A 1° square is approximately the largest region where it is feasible to plot all of the current vectors at 1/64° resolution. Fig. 5 is a snapshot of currents for layer 1 which includes a trail of eddies west of Dominica that are 10–20 km in diameter.

6. Impact of resolution on upper ocean model–data comparisons

6.1. Eddy statistics

Eddy statistics and distribution are a valuable indicator of model realism in simulating mesoscale variability, eddy dynamics, and the associated mixed baroclinic–barotropic flow instabilities and unstable currents. All of the simulations in Fig. 4 are eddy-resolving and contain eddies (even 1/4° is marginally eddy-resolving, e.g. Murphy et al., 1999), but an explosion in ubiquitous eddy activity is evident with the resolution increase from 1/8° to 1/16°. Table 5 summarizes a variety of eddy statistics as a function of model resolution. It includes some comparisons with available observations, but sufficient observational information is available for only a few comparisons.
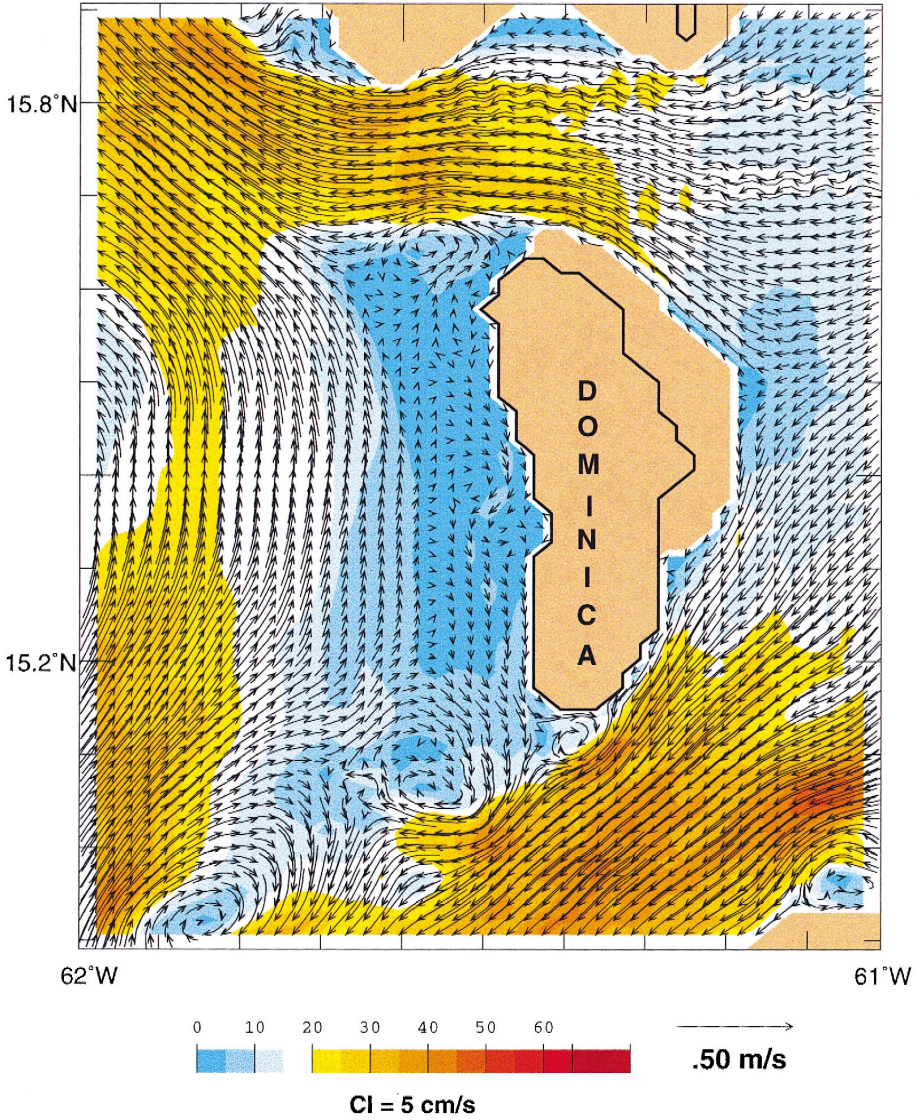
Fig. 5. Snapshot of layer one current vectors (arrows) superimposed on current speed (color) for a 1° square surrounding the island of Dominica in the Lesser Antilles island chain from 1/64°, five-layer simulation 64H in Table 1. The location is marked as a red box on Fig. 4d for reference. Every current vector on the 1/64° grid is plotted. The contour interval of the current speed is 5 cm s^{-1}.

   While both cyclonic and anticyclonic eddies are found on both sides of the Gulf Stream, they are predominantly anticyclonic on the north side and cyclonic on the south side consistent with eddy pinch off from northward and southward Gulf Stream meanders. However, as evident in Fig. 4, many eddies form without detaching from the

Gulf Stream and animations of these simulations show that the model Gulf Stream can shed both cyclonic and anticyclonic eddies on the same side of the stream, sometimes in pairs. In Table 5, under rings generated/year, only rings shed from the Gulf Stream are counted on the south side of the stream (because this is a meaningful count and it would be difficult to obtain an unambiguous count over the entire subtropical gyre), while all are counted on the north side (for comparison with Auer (1987)). Also, only eddies that are clearly separated from the Gulf Stream are used in the eddy statistics. Recirculation gyres which form in meanders (cyclonic on the north side and anticyclonic on the south side) are not counted as eddies.

Auer (1987) discusses the distribution of the formation and absorption/decay of the anticyclonic WCRs on the north side of the Gulf Stream based on 5 continuous years of satellite IR analyses, the regional eddy features best observed in the IR data. He notes maximum formation rate near the NESC (62°–65°W) decreasing to zero west of 70°W and relatively uniform formation rates from the NESC to the western side of the Grand Banks. Many of the rings are absorbed or decay near Cape Hatteras west of 71°W with a minimum 67°–71°W and relatively uniform absorption/decay eastward to the western side of the Grand Banks. This is consistent with the WCR distribution and behavior seen in the 1/16°, 1/32°, and 1/64° models where all three snapshots from these models (Fig. 4b–d) show a relatively prominent WCR near 65°W north of the Gulf Stream. The 1/64° model and statistics derived from Auer's IR analysis of WCRs on the north side of the Gulf Stream show good agreement for mean ring population and number of rings generated/year (Table 5). The values for the 1/16° model are lower. However, matching the threshold for detection between Auer's observations and rings counted in the model is a significant obstacle to obtaining an accurate comparison. Model criteria are given in footnote b of Table 5. A similar comparison for the cyclonic cold core rings (CCRs) on the south side of the Gulf Stream cannot be made because such rings can lack an SST signature.

Two ways of expressing ring diameter are quite useful, (a) diameter between speed maxima and (b) total diameter. Both are used in Table 5, expressed as *aaa/bbb*. Total diameter mean and SD values for anticyclonic rings (WCRs) on the north side of the Gulf Stream show almost exact agreement between the 1/64° model and Auer's IR analyses, and mean values at the other two resolutions agree within 25%. Two observed values for total diameter are given for CCRs on the south side of the Gulf Stream, one from satellite IR (105 km) (Auer, 1987) and one from the depth of the 15° isotherm (250 km) (Lai and Richardson, 1977). Auer explains the difference by the doming of isotherms in CCRs and by noting that he calculated the inside diameter within intruding warm filaments. In addition, the ship observations may be biased toward relatively large, prominent rings. Interestingly, the 105 km mean CCR diameter from IR agrees to within 15% with all of the model mean CCR diameters between speed maxima (and to within 25% for all of the corresponding SDs) in both regions of the subtropical gyre. This suggests a possible link between the locations of CCR speed maxima and intruding warm filaments.

With the exclusion of cyclonic eddies on the north side of the Gulf Stream, the model mean eddy diameters between speed maxima vary by < 25% about their overall mean of 101 km regardless of rotation, location or model resolution. The model cyclonic

eddies on the north side of the Gulf Stream, where the radius of deformation is smaller, have an overall mean diameter between speed maxima of 62 km. Note the model rings do not show a monotonic decrease in mean diameter as model resolution is increased, an indicator that the space scales for the flow instabilities which generate them are not shifted to larger scale at lower resolution because of increased numerical truncation error or increased eddy viscosity. This and consistency with observations indicate the model at all resolutions is reasonably representing this aspect of the flow instability process. However, the mean β_R do increase monotonically with resolution, indicating increased vortex nonlinearity in relation to linear propagation speed, and for CCRs in the nonlinear recirculation gyre, they are larger than the ''observed'' value. The ''observed'' value is one obtained by McWilliams and Flierl (1979) for a typical CCR shed from the Gulf Stream. The model also sheds some very intense, relatively short-lived rings with very

Table 5
Comparison of eddy statistics at $1/8°$, $1/16°$, $1/32°$, and $1/64°$ resolution in three regions

Resolution	Rotation	Two diameters (km), between speed maxima/total		β_R^a		Mean[b] (ring population)	Rings generated/year[b]	
		Mean	SD	Mean	SD		Rings	Modons[c]
North of the Gulf Stream between Cape Hatteras and the Grand Banks								
Observed[d]	A	−/129	−/43	–	–	3.7	17.4	–
$1/8°$	A	118/128	−/−	7.9	–	0.1		0.0
$1/8°$	C	−/−	−/−	–	–	0.0	0.0	
$1/16°$	A	103/124	18/22	14.7	5.8	1.8	11.2	0.0
$1/16°$	C	66/102	19/29	36.9	20.0	0.3	2.8	
$1/32°$	A	125/160	46/59	16.7	9.0	2.6	23.4	0.0
$1/32°$	C	67/104	28/43	40.1	18.3	0.3	3.6	
$1/64°$	A	92/129	30/42	28.9	11.4	3.0	19.8	0.2
$1/64°$	C	54/81	17/26	45.7	19.4	0.3	5.0	
Nonlinear recirculation gyre on the south side of the Gulf Stream[e]								
Observed[d]	C	−/105[f] (250)[a]	−/28[d] (−)	~13	–	–	–	–
$1/8°$	A	−/−	−/−	–	–	0.0	0.0	0.0
$1/8°$	C	113/118	−/−	6.1	–	0.1		
$1/16°$	A	105/189	17/31	9.2	3.8	1.8	4.2	1.8
$1/16°$	C	98/127	22/29	17.8	12.1	4.3	9.0	
$1/32°$	A	103/185	31/56	11.5	6.7	2.2	4.0	3.2
$1/32°$	C	106/164	34/53	21.1	13.3	7.3	18.4	
$1/64°$	A	81/154	18/34	20.1	12.1	1.6	3.5	2.8
$1/64°$	C	90/141	28/44	28.6	19.7	12.0	11.5	
Subtropical Gyre outside the nonlinear recirculation gyre[e]								
$1/8°$	A	92/125	−/−	7.2	–	0.1		
$1/8°$	C	119/158	36/36	7.8	5.3	1.4		
$1/16°$	A	102/143	23/32	7.9	4.2	0.8		
$1/16°$	C	103/124	22/26	8.3	5.7	11.8		
$1/32°$	A	90/180	35/70	16.2	16.8	0.7		
$1/32°$	C	114/129	34/38	8.8	4.7	14.3		
$1/64°$	A	78/156	15/30	18.2	10.0	2.0		
$1/64°$	C	95/124	21/27	15.8	16.4	18.0		

small diameters, as seen in Fig. 4. Some of these are included in the eddy diameter and β_R averages giving larger mean β_R values than the one calculated by McWilliams and Flierl (1979) and large SDs. The overall results for the eddy statistics and distribution are a good indicator that the five-layer models are realistically simulating mesoscale variability, eddy dynamics and the associated mixed baroclinic–barotropic instabilities.

6.2. Mean Gulf Stream pathway

Fig. 6 shows three comparisons between simulation 32H (Table 1) and observed mean Gulf Stream pathways and their envelope of variability. The observed pathways are derived from satellite IR imagery and from TOPEX/Poseidon and GEOSAT-Exact Repeat Mission (ERM) altimetry. The IR pathway is a 15-year mean (1982–1996) for the Gulf Stream north wall calculated by Z. Sirkes (personal communication) using IR analyses provided by P. Cornillion. See Cornillion (1986) and Cayula and Cornillion (1995) for the automated analysis techniques and additional analysis results. The altimetric mean pathways are for the Gulf Stream axis as determined by Lee et al. (1997). The observed and 1/32° modeled pathways are in close agreement between Cape Hatteras and the NESC ($\sim$ 65°W) and qualitatively similar (modeled generally within the observed envelope of variability) between the NESC and the Grand Banks.

Notes to Table 5:

[a] The β Rossby number, $\beta_R = v_s / \beta r^2$, where v_s is the average maximum swirl velocity around the ring, β is the rate that f (the Coriolis parameter) varies with latitude (1.8×10^{-11} m^{-1} s^{-1} was used here) and r is the average radius of the ring. The ''observed'' value is one obtained by McWilliams and Flierl (1979) for a typical cold core ring shed from the Gulf Stream.

[b] Only well-defined rings clearly separated from the Gulf Stream and strong enough to produce two closed contours on SSH plots like Fig. 4 or maximum swirl velocity averaged around the ring > 40 cm/s were counted. South of the Gulf Stream only rings shed from the Gulf Stream were used in the count of rings generated/year, but as seen in Fig. 4, many additional eddies were generated with the result that the mean ring population in the nonlinear recirculation gyre exceeds the number of rings generated/year at 1/64° resolution. At 1/8° resolution, the stronger northern Gulf Stream pathway was used in the ring generation counts.

[c] Counter-rotating vortex pairs were counted as modons only if they had an eastward component of propagation, although a few additional counter-rotating vortex pairs exhibited mutual advection with a westward component. The simulated modons counted had a typical life span of 10 days to 2 months. A particularly strong one is seen in Fig. 4d near 25°–30°N and 70°W which lasted longer than 2 months.

[d] From satellite IR (Auer, 1987) except as noted below. The mean warm core ring (WCR) population and generation per year north of the Gulf Stream were derived from Auer's Table 5, Fig. 12, and supporting comments made in the text. Only the region between the Grand Banks (50°W) and Cape Hatteras (75°W) was considered. Auer also counted cold core rings, but his count was incomplete because these rings can lack a sea surface temperature signal. Hence, that count was not used for comparison here.

[e] The nonlinear recirculation gyre was defined as the area within the general envelope of light red in Fig. 4, i.e. > 32 cm. The rest of the subtropical gyre was defined as the area within the general envelope of yellow–green (> 0 cm) excluding the nonlinear recirculation gyre, Caribbean Sea, Gulf of Mexico, Bahamas region and the region directly east of the Grand Banks.

[f] The two observed mean diameter values for cold core rings south of the Gulf Stream were obtained from satellite IR (105 km) by Auer (1987) and from the depth of the 15°C isotherm (250 km) by Lai and Richardson (1977).

In Fig. 7, the three renditions of the Gulf Stream pathway, satellite IR northwall and Gulf Stream axes from TOPEX/Poseidon and GEOSAT altimetry, are superimposed on the mean SSH from (a) 1/16°, (b) 1/32°, and (c) 1/64° simulations. The three
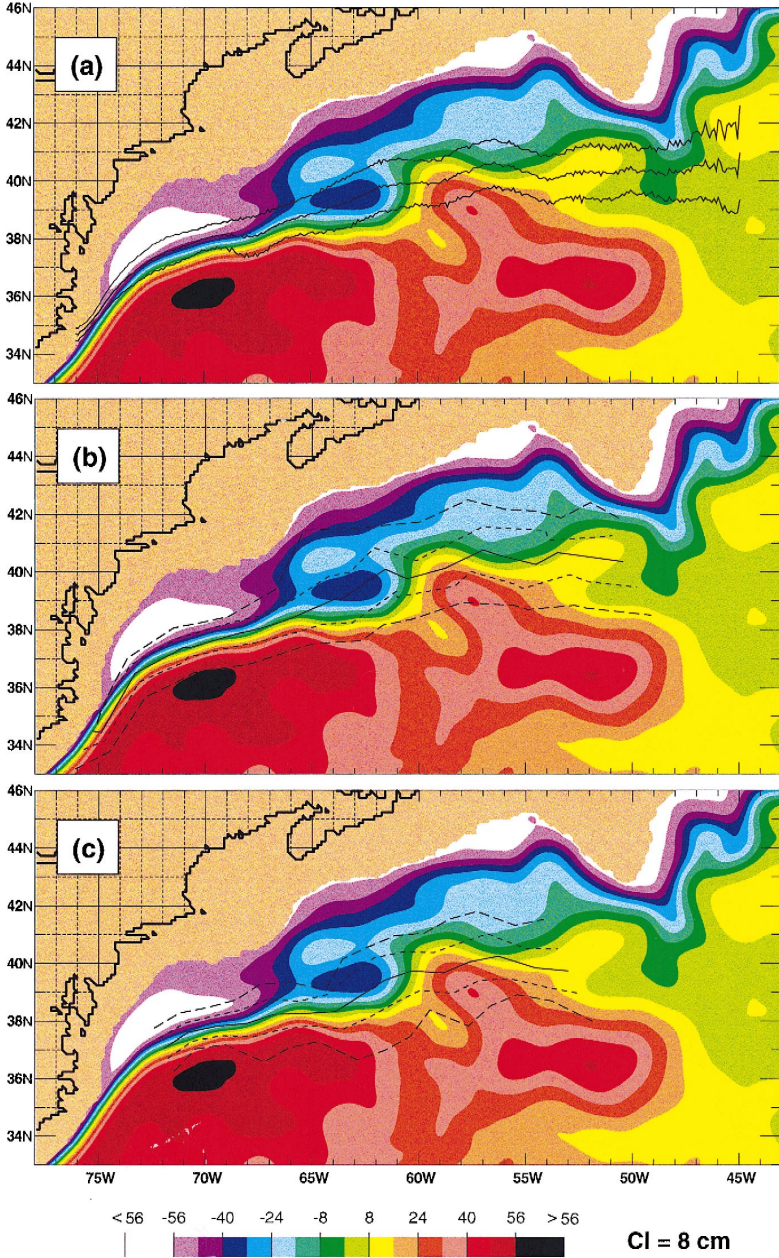
simulations show quite similar mean Gulf Stream pathways and roughly similar agreement with the observed pathways, agreement that is within the range of variation found in different simulations with the same resolution. They are all much more realistic than found in the linear (Fig. 2) and 1/8° nonlinear (Fig. 4a) simulations, which are excluded in many of the model–data comparisons because of obviously unrealistic behavior in this region. In Fig. 7, the 1/32° simulation shows the best agreement overall with the observed mean Gulf Stream pathways. As discussed in Section 5, many of our 1/16° simulations (although not 16H, Fig. 7a) overshoot the observed latitude of the Gulf Stream pathway just east of Cape Hatteras, but this has not been a significant problem in the higher resolution simulations.

West of the NESC, the three observed pathways are in close agreement, with the IR northwall pathway slightly to the north as expected. However, from cross-sectional observations of the Gulf Stream, the maximum surface current strength is also displaced north of the center of the Gulf Stream cross-section (Halkin and Rossby, 1985; Johns et al., 1995; Schmitz, 1996), although not in observations at 55°W by Richardson (1985). The 1/32° simulation west of the NESC is in close agreement with this analysis of the positioning. East of the NESC, the Gulf Stream axis from TOPEX/Poseidon (1993–1996) is north of the one determined from GEOSAT (1987–1989), even slightly north of the mean 1982–1996 IR northwall pathway, indicating an intradecadal variation in the mean path of the Gulf Stream in this region.

6.3. Mean gyre-scale circulation

Fig. 8 shows contours of the mean surface dynamic height with respect to 1000 m from the generalized digital environmental model (GDEM) oceanic climatology (Teague et al., 1990) superimposed on the mean model SSH in color from the same three simulations. This comparison is not very useful for the Gulf Stream pathway because the pathway in the climatology is so diffuse. However, it is quite useful for comparing the larger-scale features of the observed and simulated nonlinear recirculation gyres on the south side of the Gulf Stream. GDEM and all three simulations show a similar large western nonlinear recirculation gyre, an eastern nonlinear recirculation gyre with a secondary maximum, eastward penetration of the nonlinear recirculation gyre as far as 44°–48°W, evidence of a C-shape to the subtropical gyre, and roughly similar positioning for the ''C''. The western recirculation gyre is approximately the same in all three simulations. They have roughly similar features for the eastern part of the gyre, but the eastern gyre is weaker at 1/16° resolution and the center is farther to the west. Both the 1/32° and 1/64° simulations have eastern maxima within 1° of the one found in GDEM.


Fig. 6. Mean SSH (color) in the Gulf Stream region from 1/32°, five-layer simulation 32H in Table 1. Different observations of the Gulf Stream mean pathway are superimposed: (a) mean northwall of the Gulf Stream from satellite IR (middle line) flanked by lines an SD away from Z. Sirkes and P. Cornillion (personal communication); (b) mean axis of the Gulf Stream determined from TOPEX/Poseidon altimetry (solid line), along with lines an SD away (short dashed lines) and extreme positions of the axis (long dashed lines); (c) same as (b) except for the GEOSAT altimeter (both from Lee et al., 1997). The contour interval of mean SSH is 8 cm.

6.4. Mean upper ocean transports

Table 6 shows model–data and model–model comparisons of upper ocean transports for seven of the simulations listed in Table 1. The transport sections are marked on Fig.
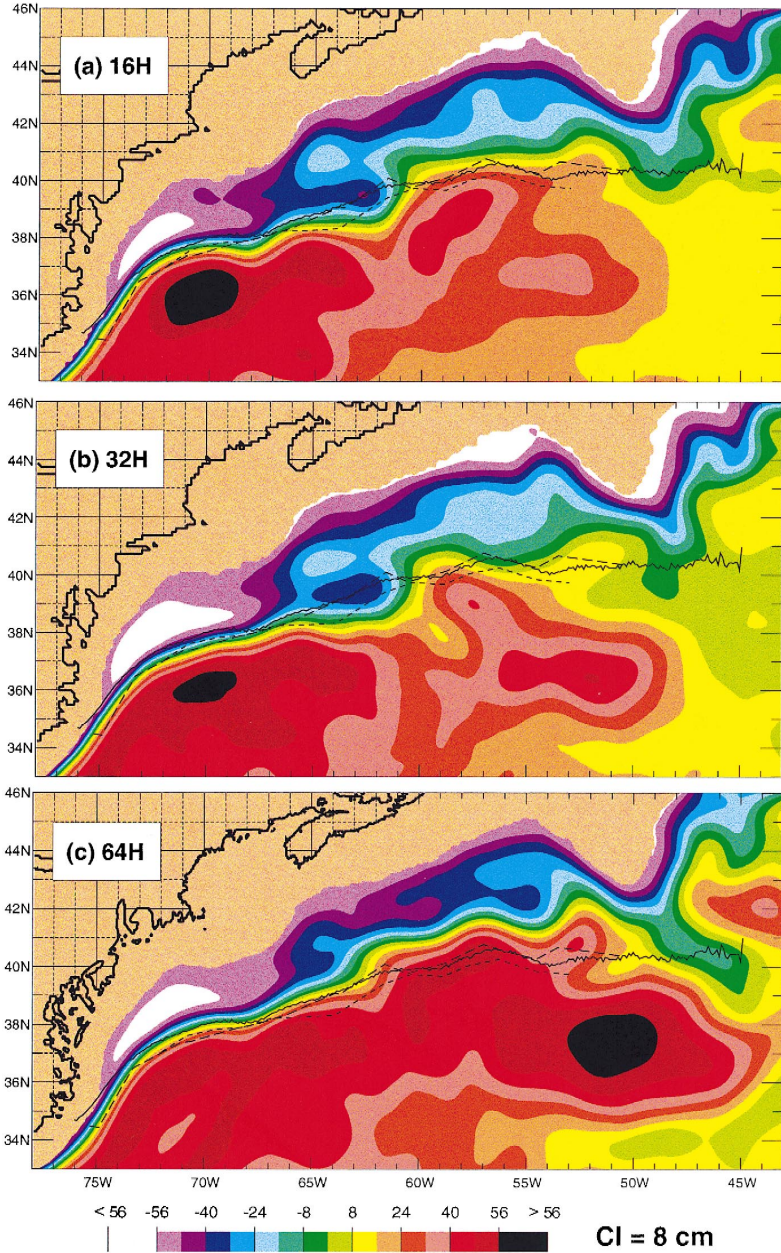
2a and were chosen to measure salient aspects of the Gulf Stream system from the Florida Straits to east of the Grand Banks. At 27°N, all of the simulations and the observations are in close agreement for the total upper ocean western boundary current transport (''sum of above'' in Table 6) and all give values that are close to Sverdrup transport plus a 13 Sv global thermohaline contribution estimated by Schmitz and Richardson (1991). In contrast, all of the nonlinear simulations show transports at Cape Hatteras which are substantially augmented by the nonlinear recirculation gyre and several show close agreement with observations by Richardson and Knauss (1971). In the 1/8° model, the nonlinear enhancement of the transport near Cape Hatteras is a localized effect due to the small size of the nonlinear recirculation gyre, which is located near Cape Hatteras (Fig. 4a).

The western boundary current transport at 38°N is designed to distinguish between simulations that separate from the coast at Cape Hatteras (transport at 38°N ≤ 0) and those which have at least part of the western boundary current transport hug the western boundary too far north. In 1/16° simulation 16H, the subtropical Atlantic simulation, the Gulf Stream is separated from the coast at 38°N while in the two 1/16° global simulations, 16GH and 16GI, it is not. All three of these 1/16° simulations and the higher resolution simulations have similar Gulf Stream pathways farther to the east and the 1/16° global simulations exhibit more realistic variability east of the NESC than the 1/16° subtropical Atlantic, as discussed shortly. Additional transports in Table 6 are designed to show impacts of the model resolution and the strength of nonlinear recirculation gyres on (a) upper ocean Gulf Stream system transports and (b) model–data comparisons farther to the east.

6.5. SSH variability

SSH variability and the eddy kinetic energy (EKE) of geostrophic surface currents are measured by satellite altimetry and are the best sampled, dynamically relevant measures of upper ocean variability available. We have chosen SSH variability as our primary model–data comparison for upper ocean variability because it is more accurately measured by satellite altimetry. In Fig. 4, we see that high variability is ubiquitous in the higher resolution simulations. However, the highest SSH variability is found where there are strong, persistent time variable features or a high density of very strong eddies, usually spawned by the former. In the Gulf Stream region such features include the Gulf Stream and North Atlantic Current, the western and eastern nonlinear recirculation gyres on the south side of the Gulf Stream, the nonlinear recirculation gyre east of the Grand Banks and eddy fields generated by these features, especially cold eddies south of the

---

Fig. 7. Mean SSH (color) in the Gulf Stream region from (a) 1/16° simulation 16H, (b) 1/32° simulation 32H, and (c) 1/64° simulation 64H. Superimposed on each is the mean northwall of the Gulf Stream as determined from satellite IR imagery (solid line), and the mean Gulf Stream axis from TOPEX/Poseidon altimetry (long dashed line) and GEOSAT altimetry (short dashed line). The contour interval for the mean SSH is 8 cm. Observational credits as in Fig. 6. Note added in final: in a subsequent 1/64° simulation, the accuracy of the Gulf Stream pathway between the NESC and the Grand Banks was improved by a 3/4° displacement to the south. See footnote d in Table 6.
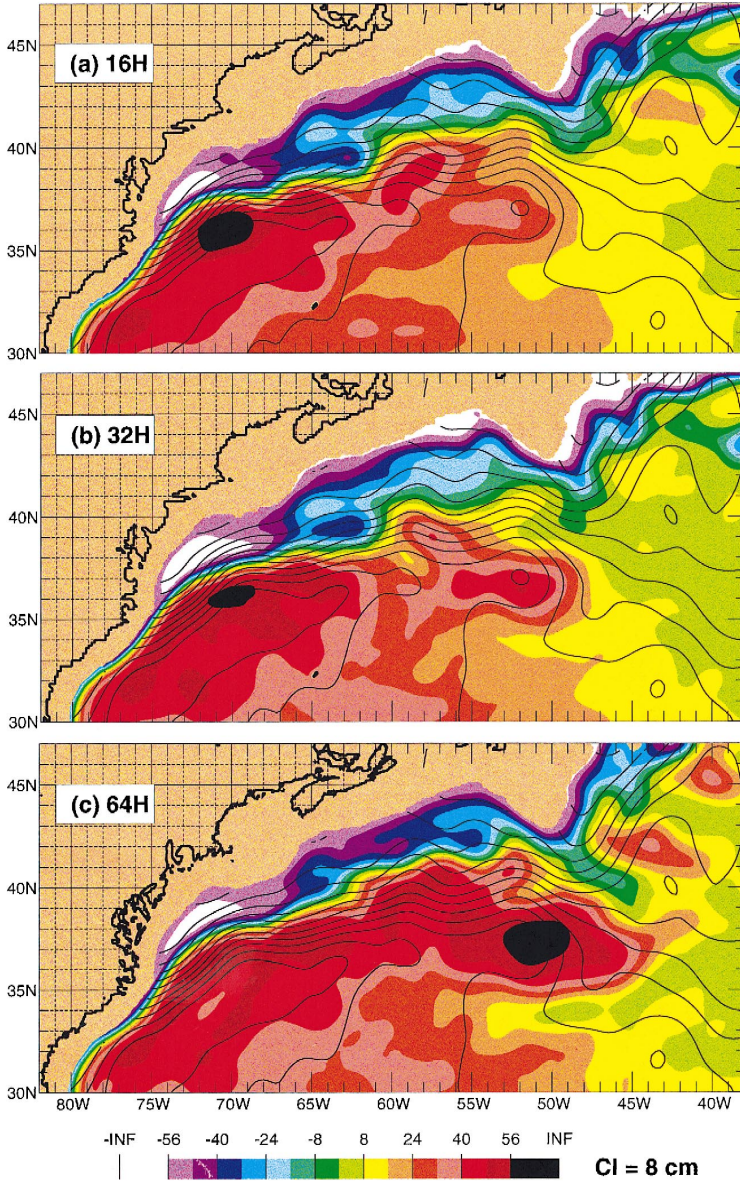
Fig. 8. Mean SSH (color) in the Gulf Stream region from (a) $1/16°$ simulation 16H, (b) $1/32°$ simulation 32H, and (c) $1/64°$ simulation 64H. Superimposed on each are contours of surface dynamic height with respect to 1000 db from the Navy's GDEM oceanic climatology (Teague et al., 1990). Contour interval for the surface dynamic height and the model mean SSH is 8 cm.

Gulf Stream (but also some warm ones) and warm eddies north of the Gulf Stream. The strong features seen in the SSH variability from TOPEX/Poseidon (Fig. 9f) and the

Table 6
Mean upper ocean transport in Sv, simulated vs. observed at selected locations

	Simulated							Observed[a]
	16LH + T[b]	8H	16H	16GH	16GI[c]	32H	64H[d]	
Florida Straits at 27°N[e]	39	31	29	29	30	36	27	32
East of Abaco Island at 26.5°N	−1	8	5	8	7	2	9	5
Sum of above[f]	38	39	34	37	37	38	36	37
Gulf Stream at Cape Hatteras	39	52	58	61	62	64	62	63
Western boundary current at 38°N[g]	22	20	−4	28	30	−4	−3	−7 (S)
Gulf Stream at 68°W[h]	17	10	60	64	64	63	60	68 and 80[i]
N. Atlantic Current, west of Grand Banks[j]	0	1	9	8	8	13	9	15 (S)
S. of Grand Banks to 36°N[k]	26	29	36	49	49	49	59	70 (S)
N. Atlantic Current, east of Grand Banks at 44°N	23	23	19	25	29	23	23	38 (S)

[a] Observed values were obtained from Richardson and Knauss (1971), Hogg (1992), Larsen (1992), Johns et al. (1995), Lee et al. (1996), and Schmitz (1996). (S) denotes values from schematics by Dietrich et al. (1980), Schmitz and McCartney (1993), and Schmitz (1996). Transports are positive eastward and northward, negative westward and southward.

[b] See Table 1 for the list of simulations. + T means a 13 Sv contribution from the upper ocean branch of the global thermohaline circulation (Schmitz and Richardson, 1991) was added to the western boundary current transport of the linear simulation. That contribution is already present in the nonlinear simulations.

[c] Transports averaged over 1990–1996 from simulation 16GI.

[d] Note added in final: in simulation 64H, the Florida Straits transport is lower than observed, although the total western boundary current transport at 27°N (sum of above) is realistic. This was subsequently traced to a subsill friction parameter change in the Florida Straits. When this value was restored to the value used in simulation 32H, the Florida Straits transport at 27°N became 32 Sv, the transport east of Abaco Island became 7 Sv, and the Gulf Stream transport at Cape Hatteras remained 62 Sv. The simulation of the Gulf Stream system between Cape Hatteras and the Grand Banks is similar to 64H, but the simulated Gulf Stream pathway between the NESC and the Grand Banks is more accurate, about 3/4° farther south. See Fig. 7.

[e] Sections marked on Fig. 2. Transports exclude the abyssal layer.

[f] Measure of total upper ocean western boundary current transport at 27°N.

[g] Strength of unrealistic Gulf Stream pathway when positive and the strength of a nonlinear recirculation gyre on the north side of the Gulf Stream when negative.

[h] Simulations 8H and 16LH + T exhibit two Gulf Stream pathways at 68°W, while all of the others have only one. For simulations 8H and 16LH + T, only the transport of the southern branch is included at 68°W. For these two simulations, it is useful to have separate measurements of the transports in each branch, the western boundary current transport at 38°N for the northern branch and the transport at 68°W for the southern one.

[i] Value of 68 Sv from Hogg (1992), baroclinic + barotropic transport in the top 1000 m and value of 80 Sv in the upper 1000 m from Johns et al. (1995).

[j] 43.0°N, 53.9°W to 44.0°N, 52.5°W (shelf break and model boundary). Positive southeastward.

[k] Total eastward transport south of the Grand Banks at 50°W; North Atlantic Current + Gulf Stream and nonlinear recirculation gyre, excluding the abyssal layer.

model simulations (Fig. 9a–e) can be explained in terms of these phenomena. The ability of the different simulations to reproduce the variability associated with specific features can thus be assessed. To facilitate the assessment, the mean Gulf Stream axis and the envelope of variability from TOPEX/Poseidon altimetry (Lee et al., 1997) have been superimposed on each panel in Fig. 9.

CI = 2 cm
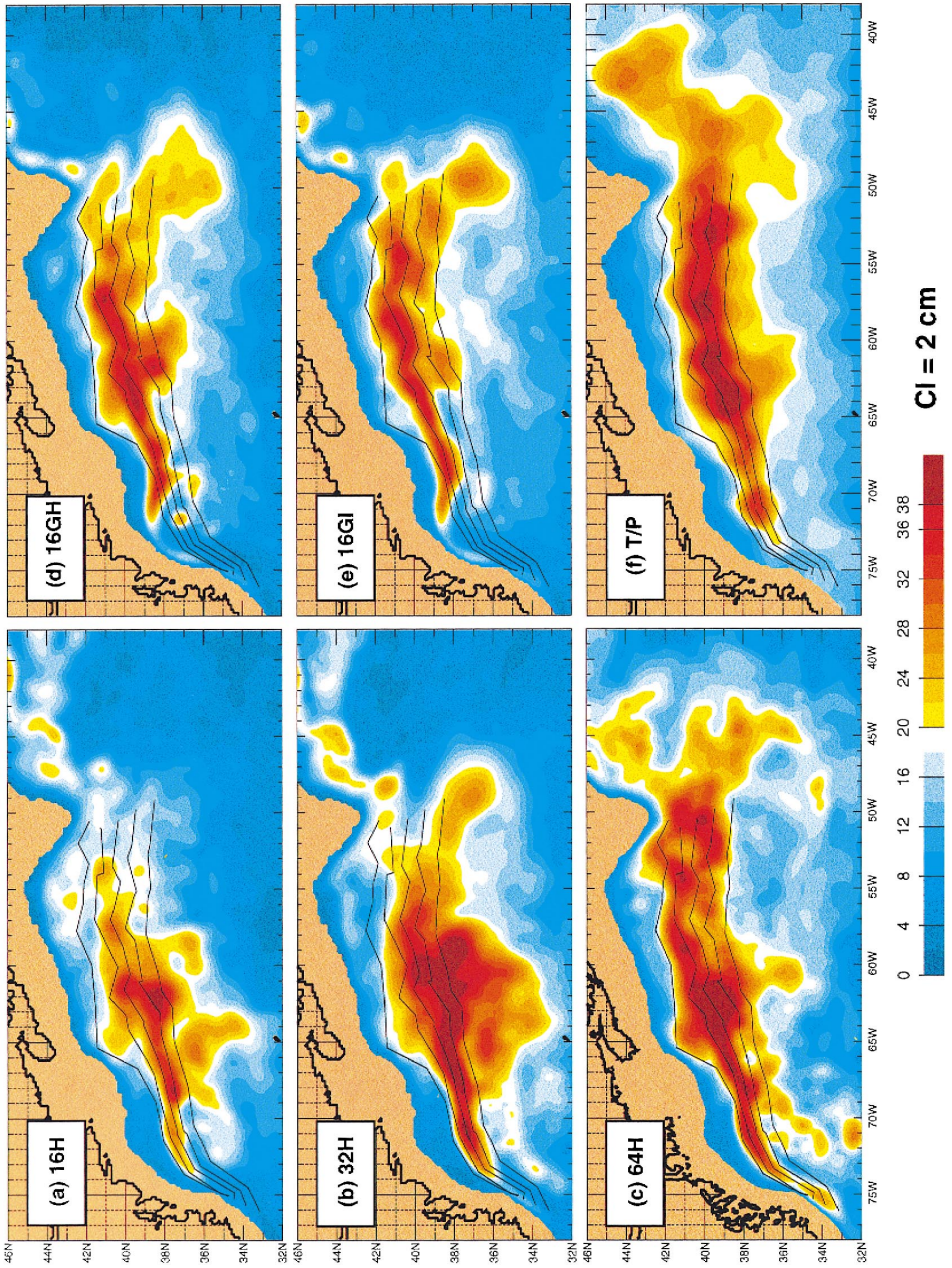
The highest SSH variability is expected along the axis of the Gulf Stream between Cape Hatteras and the Grand Banks because it is the strongest, highly time variable feature in the region. However, in most regions the strongest SSH variability measured by TOPEX/Poseidon is south of the Gulf Stream axis from TOPEX/Poseidon analyzed by Lee et al. (1997). This is consistent with observations that the maximum strength of the Gulf Stream surface current is displaced north of the center of the Gulf Stream cross-section (Halkin and Rossby, 1985; Johns et al., 1995; Schmitz, 1996), although not in observations at 55°W by Richardson (1985). Generation of strong CCRs on the south side of the Gulf Stream and the eastern nonlinear recirculation gyre may also contribute to this. While an excellent data set for model–data variability comparisons, the TOPEX/Poseidon variability map has some limitations in addition to the 4-year (1993–1996) data record length, a topic investigated by Hogan et al. (1992) using simulated altimeter data for the Kuroshio from a 1/8° Pacific Ocean model. The altimetric resolution is too coarse to represent or perhaps even see some of the smaller scale features found in the model simulations. In addition, the optimum interpolation to a uniform grid shows some smearing, blobbing, and scalloping characteristics. In comparison with an along track variability analysis (not shown), the amplitude of sharp peaks tends to be reduced.

West of about 68°W, there are three main features of note seen in the altimetry and all of the simulations with some variation. These are (1) a narrow band of high variability along the Gulf Stream axis, (2) a weaker band of variability paralleling it to the south along a preferred pathway for Gulf Stream rings (see Fig. 4), and (3) low SSH variability north of the Gulf Stream, even though WCRs are found in that region. In the 1/16° global simulations (Fig. 9d,e), the variability in this region associated with the Gulf Stream axis is substantially too far north because the Gulf Stream pathway is too far north. Close to Cape Hatteras and to the south the SSH variability along the Gulf Stream axis is greatly reduced in all but the 1/64° simulation, which shows more meandering and interaction with eddies in that region than the other simulations. T/P and most of the other simulations show a lower amplitude relative maximum in that region.

East of about 65°W, the corridor of high variability broadens greatly in all of the simulations and the observations, especially in the vicinity of the NESC where increased meandering and eddy generation is found in the simulations. Another southward bulge in SSH variability is found between 45° and 50°W at the eastern end of the eastern lobe of the nonlinear recirculation gyre. It is seen in the altimetry and all of the simulations, but

Fig. 9. SSH variability (color) in the Gulf Stream region from (a) 1/16° five-layer Atlantic simulation 16H, (b) 1/32° five-layer Atlantic simulation 32H, (c) 1/64° five-layer Atlantic simulation 64H, (d) 1/16° six-layer global simulation forced by HR monthly climatological winds (simulation 16GH), (e) 1/16° six-layer global simulation over 1990–1996 that was forced by interannual winds as described in Section 3 and Table 1 (simulation 16GI), and (f) TOPEX/Poseidon altimetry over the time period 1993–1996. All of the simulations also included constant global thermohaline forcing (see Section 3 and Table 2). Superimposed on each is the mean (center line), lines an SD away from the mean on either side and extreme (outer lines) of the Gulf Stream axis as determined from TOPEX/Poseidon altimetry by Lee et al. (1997). The contour interval of the SSH variability is 2 cm.

only weakly in simulation 16H and with some westward displacement in all but the 1/64° simulation (64H). In all cases, there is evidence of a westward tongue of variability wrapping around the gyre from the eastern to the southern side. On the northern side of the nonlinear recirculation gyre, the altimetry shows a corridor of high variability near 40°N paralleling the Gulf Stream axis. The RMS SSH variability along this corridor exceeds 20 cm past 44°W. All of the simulations show a similar corridor of variability, but it is best represented in simulation 64H in terms of amplitude, latitude, and eastward penetration (> 20 cm amplitude past 44°W near 40°N as observed). All of the other simulations have it too weak, too far north and with insufficient eastward penetration.

East of the Grand Banks, the altimetry shows high variability in the region of a nonlinear recirculation gyre which Schmitz and McCartney (1993) show schematically as having a transport of 25 Sv. All of the simulations show evidence of an anticyclonic gyre in this region, but only the 1/64° model shows evidence of developing a substantial nonlinear recirculation gyre and the associated high variability in this region, and it is weaker than observed.

The 1/64° simulation, 64H (Fig. 9c) easily exhibits the most realistic pattern of variability in comparison to T/P, and overall 1/16° simulation, 16H the least realistic. A comparison of the three 1/16° simulations shows a much more realistic pattern of variability in the two global simulations east of about 60°W even though the global simulations have a less realistic Gulf Stream pathway just east of Cape Hatteras. South of the Grand Banks, the two 1/16° global simulations and simulation 64H show the most realistic pattern and amplitude for SSH variability even though simulations 16H and 32H are the best of many simulations and these three simulations are unique or the best of a few. In addition, simulations 16H and 32H show a corridor of relatively high variability along 44°N due to the model boundary at 47°N. This is absent in the global simulations and in simulation 64H, where the northern model boundary was moved to 51°N. Comparing the two global simulations, 16GH and 16GI, we see that the SSH variability is noticeably increased (∼ 4 cm) in two regions by the interannual wind forcing. One is at the eastern end of the nonlinear recirculation gyre (the southward bulge south of the Grand Banks) and the other is the large blue area south of the Gulf Stream between 50° and 65°W.

7. Effects of resolution on simulated abyssal circulation and abyssal model–data comparisons

There are two main driving mechanisms for the abyssal layer mean flow in the model simulations, the DWBC and mixed baroclinic–barotropic flow instabilities, which efficiently transfer energy downward to the abyssal layer. The DWBC is driven via ports in the northern and southern model boundaries (Table 2). The impact of model resolution on the abyssal layer mean flow is dramatically illustrated in Fig. 10 using the mean abyssal layer pressure field (mean pressure deviation from a model ocean at rest).

At 1/8° resolution, the DWBC is the principal mean abyssal layer flow and is seen following the continental slope shown in Fig. 1. The eddy-driven mean abyssal gyres are
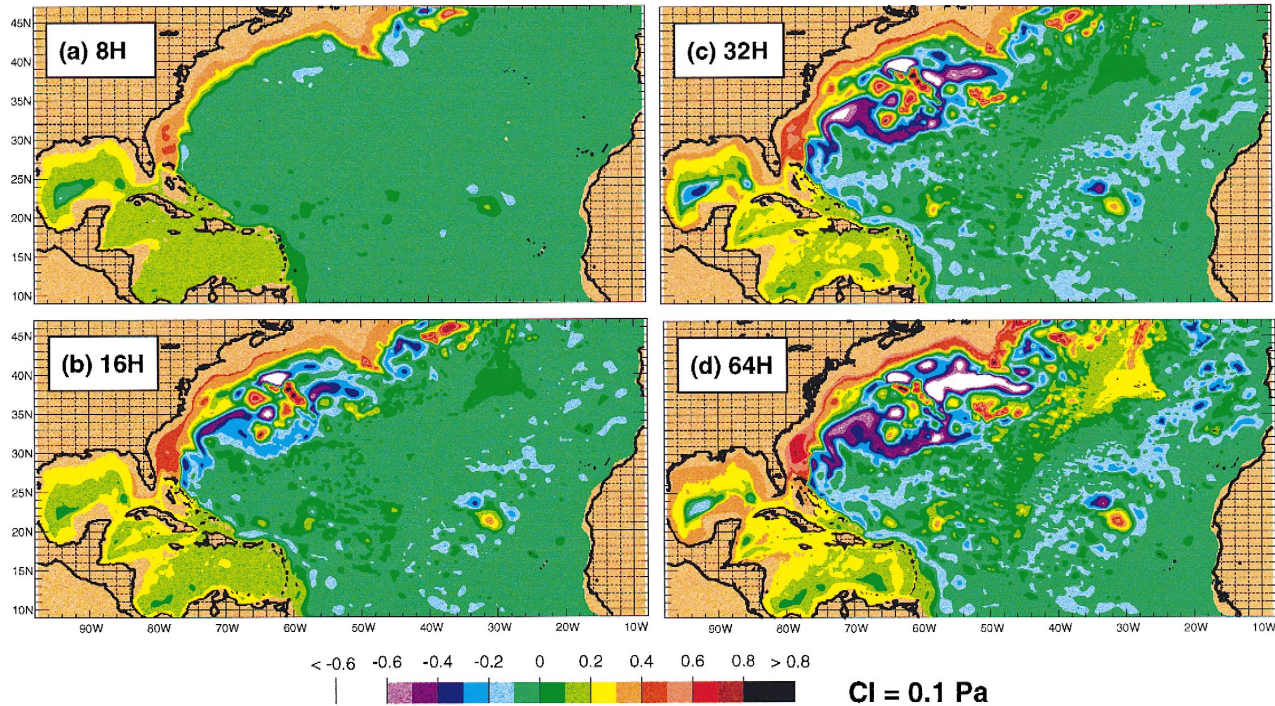
Fig. 10. Whole domain mean abyssal layer pressure deviation (from the rest state) from five-layer Atlantic subtropical gyre experiments with horizontal grid resolution of (a) 1/8° (simulation 8H), (b) 1/16° (simulation 16H), (c) 1/32° (simulation 32H), and (d) 1/64° (simulation 64H). Contour interval of mean density–normalized pressure deviation is 0.1 m² s⁻². Note the abyssal layer circulation patterns are strongly influenced by the f/h contours of the bottom topography shown in Fig. 1. For example, the NESC is plainly outlined at the three higher resolutions.

few and weak. In contrast, strong eddy-driven closed circulations are seen at all the higher resolutions. The strength of these circulations increases as the resolution is increased from $1/16°$ to $1/32°$, but less so from $1/32°$ to $1/64°$. In some regions, we see evidence of solution convergence in this field with the increase to $1/64°$ resolution, although substantial differences in detail are also seen. Comparison to the bottom topography (Fig. 1) shows that the eddy-driven mean abyssal flows at the three higher resolutions are strongly influenced by the f/h contours of the bottom topography, e.g. anticyclonic flow around the New England Seamounts.

The eddy-driven mean abyssal flow has a strong influence on the pathways of the DWBC, especially in the region east of Cape Hatteras. This is also shown in Fig. 11 for $1/32°$ simulation 32H where Fig. 11a shows the mean abyssal currents and 11b shows mean abyssal layer transports per unit width, both superimposed on their strength. Since model layer 5 covers the abyssal ocean below about 1000 m, the abyssal circulation patterns shown in Fig. 11 are depth-averaged (Fig. 11a) or depth-integrated (Fig. 11b) below that depth. In all of the abyssal-flow renditions (Figs. 10 and 11), it is easy to follow a primary DWBC pathway from the northern model boundary to about 70°W and again south of 30°N. However, between these locations, the DWBC takes at least two pathways at $1/16°$ resolution or higher. Starting next to the model western boundary, between 33°N and 70°W, we see a weak, narrow and relatively shallow branch of the DWBC following the boundary. To the east, we can see a stronger branch of the DWBC, which primarily continues to follow the continental slope in simulation 64H. However, in simulations 16H and 32H, it retroflects to the east near 70°W when it encounters an eddy-driven abyssal gyre. In their schematic of abyssal thermohaline circulation pathways, Schmitz and McCartney (1993) (their Fig. 12a) show both a DWBC retroflection pathway and one that continues along the continental slope. In simulations 16H and 32H the DWBC retroflection takes multiple circuitous pathways among a variety of eddy-driven abyssal gyres until it emerges as a single strong westward current near 67°W and 35°–36°N. This branch then joins the filamented nearshore branch at 30°N in simulation 64H as well as in 16H and 32H. See Table 7 for model-simulated transports of these two DWBC branches and their confluence, and Fig. 11b for the location and context of these sections.

At $1/16°$ resolution and higher, there is another apparent southern DWBC route from near the southern part of the Grand Banks to the point where all the branches of the DWBC join at 30°N. It is part of the clearly defined westward current which emerges

---

Fig. 11. From $1/32°$ simulation 32H: (a) mean abyssal (layer 5) current vectors (arrows) and kinetic energy of the mean flow (color) in $m^2 s^{-2}$ or mean current speed in $cm s^{-1}$, and (b) mean abyssal transport vectors per unit width (arrows) and their magnitude (color) in $m^2 s^{-1}$. The magnitudes in color on (a) and (b) are plotted on a Log_{10} scale with a log contour interval of 0.125. The transport sections for Table 7 are marked on (b). Since model layer 5 covers the abyssal ocean below $\sim$ 1000 m depth, note that this figure shows depth-averaged or depth-integrated patterns below that depth. In comparison with Fig. 10, also note that while the abyssal layer circulation patterns are generally similar at the three higher resolutions, they differ substantially in detail. For example, simulations 16H and 32H show a retroflection of the DWBC to the east near 70°W while in simulation 64H, the DWBC primarily continues to follow the continental slope. In their schematic of abyssal thermohaline circulation pathways, Schmitz and McCartney (1993) (their Fig. 12a) show both a DWBC retroflection pathway and one that continues along the continental slope.

from the complex gyre structure at 35°–36°N, 67°W. A similar pathway is shown in the Schmitz and McCartney (1993) (their Fig. 12a) schematic of the abyssal thermohaline
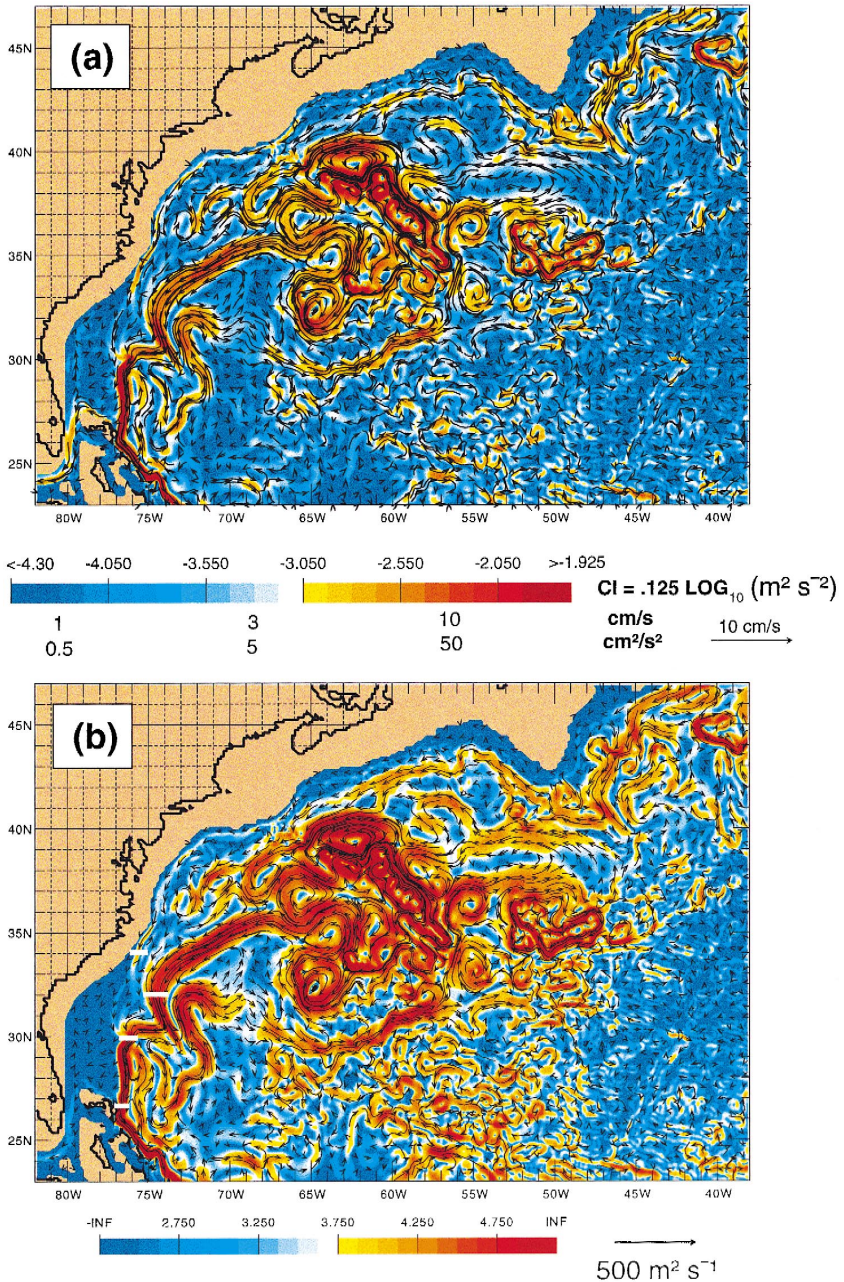
Table 7
Mean abyssal layer transports in Sv, simulated vs. observed at selected locations

	Simulated[a]				Observed[b]
	8H	16H	32H	64H	
DWBC nearshore branch at 34°N[c]	−6	−3	−3	−8	N/A
DWBC branch offshore at 32°N, 75.3°–73.8°W	−16	−30	−38	−32	N/A
DWBC confluence at 29.8°N	−15	−25	−29	−32	N/A
DWBC east of Abaco Island at 26.5°N	−17	−29	−34	−33	−40

[a] All transports are positive eastward and northward, negative westward and southward. DWBC transports specified at the northern and southern boundaries of the model domain (Table 2): 14 Sv in at the northern boundary, 13 Sv out through the southern boundary, 1 Sv upwelled to the upper ocean within the model domain.
[b] Observed value from Lee et al. (1996). N/A = not available.
[c] Transport sections are marked on Fig. 11b.

circulation. However, the abyssal layer pressure fields at the three higher resolutions indicate that in the model it is really the northern boundary of an elongated cyclonic abyssal gyre. This gyre is marked by blues and purples in the mean abyssal layer pressure fields of simulations 16H, 32H, and 64H (Fig. 10).

The best measured value of DWBC transport within the model domains is 40 Sv east of Abaco Island at 26.5°N (Lee et al., 1996). The 1/8° model shows only 3–4 Sv more than the 13–14 Sv port-driven DWBC transport at this location. However, the higher resolution simulations show transports approaching the observed mean value due to augmentation of the transport by the eddy-driven abyssal gyres (Table 7, Figs. 10 and 11).

Figs. 12 and 13 provide a model–data comparison for abyssal EKE at the four different model resolutions. Note that all of these simulations were forced by the HR monthly wind stress climatology and that the observations are at ∼4000 m depth while the model values are for a depth–average flow below 1000 m. Despite this, the model and observed values show surprisingly good quantitative agreement at the higher resolutions.

Consistent with Figs. 4 and 10, there is a dramatic increase in abyssal EKE from 1/8° to 1/16° resolution, a further increase at 1/32° and a small increase at 1/64°. The dominant dissipation mechanism in the abyssal layer changes from lateral friction to quadratic bottom friction with the resolution increase from 1/8° to 1/16°. Unlike the eddy viscosity (A, Table 1), the bottom friction coefficient (C_b, Table 2) is not changed when the model resolution is increased. This tends to restrain the abyssal EKE increases when the resolution is increased beyond 1/16°.

The observations and the three higher resolution simulations all show, by far, the highest EKE in the northwest portion of the domain beneath the dynamically unstable flow associated with the Gulf Stream system. This includes several noteworthy features seen in both the observations and the three higher resolution simulations, e.g. (1) a tongue of high variability at ∼68°–72°W which extends west–southwestward from east of Cape Hatteras to the Bahamas along the elongated cyclonic mean abyssal gyre in the region, (2) a peak in variability in the vicinity of the NESC, (3) a southward extension
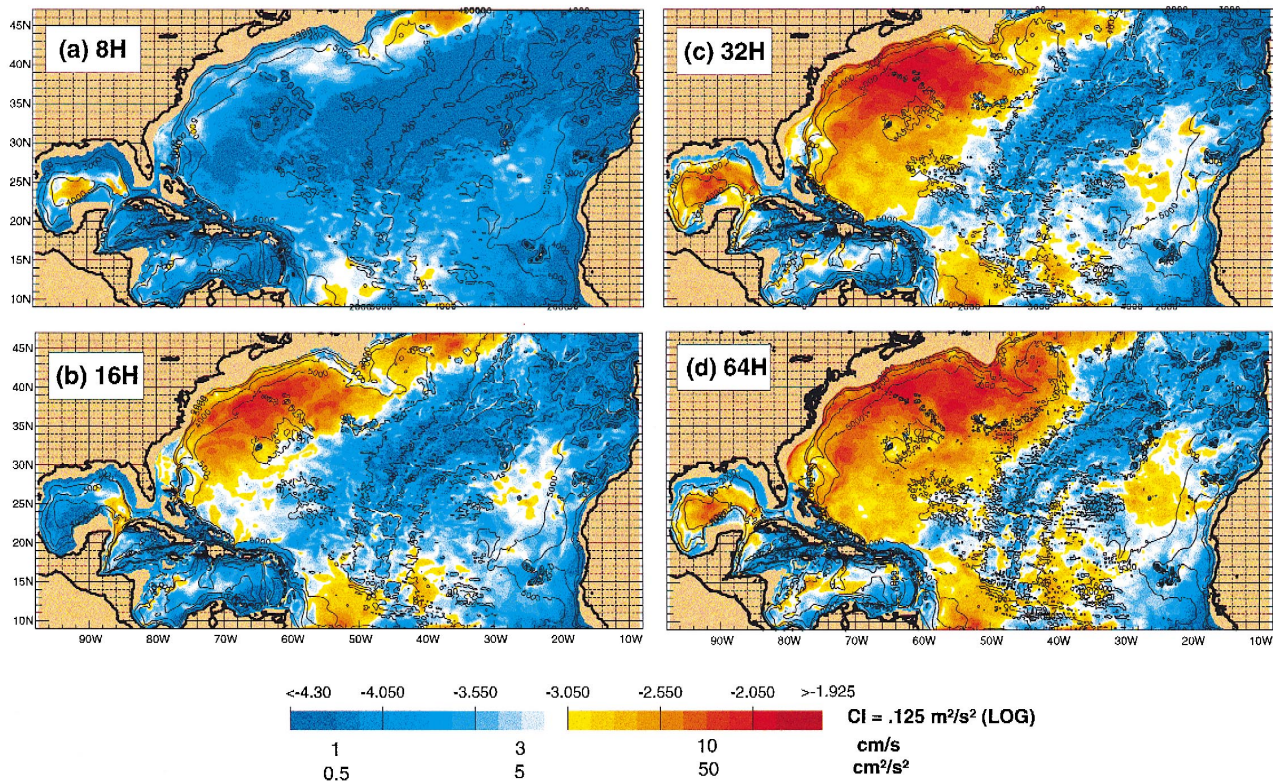
Fig. 12. Whole domain abyssal EKE from Atlantic subtropical gyre simulations with horizontal grid resolution of (a) $1/8°$ (simulation 8H), (b) $1/16°$ (simulation 16H), (c) $1/32°$ (simulation 32H), and (d) $1/64°$ (simulation 64H). The contour interval for EKE is 0.125 Log_{10} (m^{-2} s^{-2}).
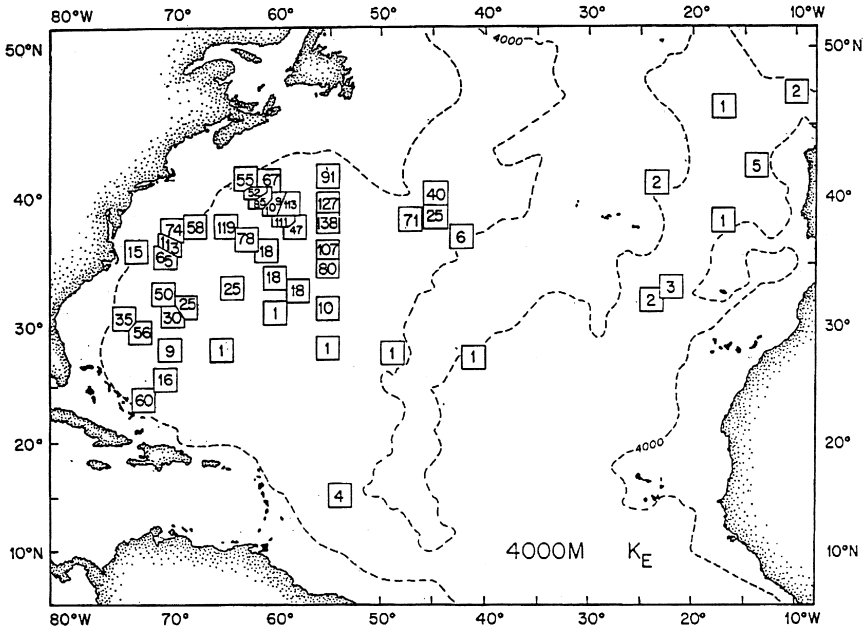
Fig. 13. . Abyssal (∼ 4000 m depth) EKE (cm^2 s^{-2}) in the Atlantic Ocean determined from current meter data (from Schmitz, 1984, 1996).

of high variability along ∼ 55°W over the Sohm abyssal plain, and (4) an eastward tongue of high EKE along 37°–40°N which terminates rather abruptly near 38°W to 45°W.

8. Summary and conclusions

In this paper, we have investigated the impact of 1/8° to 1/64° model resolution on model–data comparisons for the Gulf Stream system mainly in the region between the Florida Straits and the Grand Banks. This includes the Gulf Stream pathway, the associated nonlinear recirculation gyres, the large-scale C-shape of the subtropical gyre and the abyssal circulation. Since different ocean modelers use substantially different methods for determining grid resolution, Table 4 provides a comparison of different methods to facilitate comparisons with results from other models.

Linear solutions forced by different wind sets consistently show two unrealistic mean Gulf Stream pathways in the region between Cape Hatteras and the Grand Banks, one proceeding due east from Cape Hatteras and a second one continuing northward along the western boundary until forced eastward by the regional northern boundary (Section 4 and Townsend et al., 2000, this issue). Dynamically, these linear simulations are essentially the same as Munk (1950) with a Sverdrup (1947) interior calculated using realistic wind forcing and model boundaries, including islands. Townsend et al. (2000,

this issue) show that the northern pathway is augmented when a linear version of the upper ocean global thermohaline contribution to the Gulf Stream is included as a Munk (1950) western boundary layer driven via ports in the northern and southern boundaries of the model domain. Clearly, a major change is required to get from the two unrealistic linear Gulf Stream pathways to a realistic nonlinear pathway between Cape Hatteras and the Grand Banks.

In addition to the linear dynamics and nonlinearity, the nonlinear simulations add more layers, the barotropic mode, bottom topography, diapycnal mixing and the possibility of isopycnal outcropping. The global thermohaline contribution, mainly the upper ocean contribution to the Gulf Stream and the DWBC, is included via ports in the northern and southern model boundaries. Dynamically, the nonlinear simulations add more vertical structure to the circulation (including an abyssal circulation that can be very different from the upper ocean circulation) and the potential for meridional overturning, inertial jets, flow instabilities, eddy-driven abyssal currents, topographic steering of abyssal currents, and steering of upper ocean currents by topographically constrained abyssal currents, such as the DWBC and the eddy-driven abyssal currents. These topics will be discussed in a future paper in relation to Atlantic simulations like these.

The model simulations were performed using the NLOM which has a free surface and Lagrangian layers in the vertical that are isopycnal in these simulations. Most of the nonlinear model simulations used here have five layers in the vertical and cover the Atlantic from 9°N to 47°N or 51°N, including the Caribbean and Gulf of Mexico. Two 1/16° six-layer global simulations were also used in some of the comparisons. All were initially spun up from rest to statistical equilibrium, then extended to statistical equilibrium at progressively higher resolution.

The nonlinear Atlantic simulations were performed at 1/8° (14 km), 1/16° (7 km), 1/32° (3.5 km) and 1/64° (1.8 km) resolutions (Table 1). All are eddy resolving in the sense that they exhibit mesoscale flow instabilities and eddies. However, at 1/8° resolution, the nonlinearity and flow instabilities are not strong enough to have a large impact on the mean flow, with a few temporary exceptions such as shown by Thompson et al. (1992). At 1/8°, we mainly see a wiggly version of the two unrealistic linear pathways for the Gulf Stream. In this study, we have used model–data comparisons to investigate whether we could get realistic nonlinear simulations of the Gulf Stream system simply by increasing the horizontal resolution and decreasing the eddy viscosity, as permitted by the resolution increases.

At all the higher resolutions, we find major improvement over the linear and 1/8° nonlinear simulations, additional major improvement by increasing the resolution from 1/16° to 1/32° and evidence of simulation convergence with the increase from 1/32° to 1/64°, but with further improvement in some respects, particularly in the vicinity of the Grand Banks. The improvements include (1) realistic separation of the Gulf Stream from the coast at Cape Hatteras and a realistic Gulf Stream pathway between Cape Hatteras and the Grand Banks based on comparisons with Gulf Stream pathways from satellite IR and from GEOSAT and TOPEX/Poseidon altimetry (but 1/32° resolution was required for robust results), (2) realistic eastern and western nonlinear recirculation gyres (which contribute to the large-scale C-shape of the subtropical gyre) based on

comparisons with mean surface dynamic height from the GDEM oceanic climatology and from the pattern and amplitude of SSH variability surrounding the eastern gyre as seen in TOPEX/Poseidon altimetry, (3) realistic upper ocean and DWBC transports based on several types of measurements, (4) patterns and amplitude of SSH variability which are generally realistic compared to TOPEX/Poseidon altimetry, but which vary from simulation to simulation for specific features and which are most realistic overall in the $1/64°$ model, (5) realistic statistics for WCRs north of the Gulf Stream based on comparison to IR analyses (most realistic at $1/64°$ resolution for mean population and rings generated/year), and (6) realistic patterns and amplitude of abyssal EKE in comparison to historical measurements from current meters. Between the Florida Straits and Cape Hatteras model–data and model–model comparisons for total upper ocean western boundary current transport show a marked change from nearly linear to strongly nonlinear values. Near 27°N, there is close agreement between the observed transport, all of the model simulations, and Sverdrup transport plus a 13 Sv global thermohaline contribution. At Cape Hatteras, there is an $\sim 60\%$ nonlinear augmentation of the transport due to the nonlinear recirculation gyre on the southern side of the Gulf Stream and model agreement with observations only for nonlinear models with $1/16°$ resolution and finer.

The increase from $1/8°$ to $1/16°$ resolution also results in a basin wide explosion in the number and strength of mesoscale eddies, with additional modest increases in the population and amplitude at even higher resolutions. However, the associated RMS SSH variability is much less than the SSH variability which extends from Cape Hatteras to east of the Grand Banks due to the Gulf Stream, large nonlinear recirculation gyres south of the Gulf Stream, Gulf Stream rings and the nonlinear recirculation gyre east of the Grand Banks. Overall, the $1/64°$ model is the most successful in reproducing this variability.

The models give realistic eddy diameters at all resolutions based on IR and in situ observations and realistic β_R numbers (a measure of vortex nonlinearity in relation to linear propagation speed) at $1/16°$ resolution and higher. WCRs north of the Gulf Stream are the regional eddy features best observed by satellite IR. In comparison with IR analyses by Auer (1987), the models with $1/16°$ resolution and higher give realistic eddy statistics for WCR generation and mean population (low at $1/16°$ resolution and most realistic at $1/64°$ resolution) and they give realistic distribution of ring generation and absorption/decay. These results are a good indicator that the five-layer models are realistically simulating mesoscale variability and the associated mixed baroclinic–barotropic flow instabilities.

In general, the results of this study demonstrate that sufficient resolution is critical for realistic simulations of the Gulf Stream system. Fairly realistic simulations were obtainable at $1/16°$ resolution, but major improvement was found up to $1/32°$ resolution, and more modest improvement with a further increase to $1/64°$ resolution.

Acknowledgements

References

Auer, S.J., 1987. Five-year climatological survey of the Gulf Stream system and its associated rings. J. Geophys. Res. 92, 11709–11726.

Bleck, R., Rooth, C., Hu, D., Smith, L.T., 1992. Salinity-driven thermohaline transients in a wind- and thermohaline-forced isopycnic coordinate model of the North Atlantic. J. Phys. Oceanogr. 22, 1486–1505.

Brown, J.A. Jr., Campana, K.A., 1978. An economical time-differencing system for numerical weather prediction. Mon. Weather Rev. 106, 1125–1135.

Bryan, F.O., Böning, C.W., Holland, W.R., 1995. On the midlatitude circulation in a high-resolution model of the North Atlantic. J. Phys. Oceanogr. 25, 289–305.

Carnes, M.R., Fox, D.N., Rhodes, R.C., Smedstad, O.M., 1996. Data assimilation in a North Pacific Ocean monitoring and prediction system. In: Malanotte-Rizzoli, P. (Ed.), Modern Approaches to Data Assimilation in Ocean Modeling vol. 67 Elsevier, Amsterdam, pp. 319–345.

Cayula, J.F., Cornillion, P., 1995. Multi-image edge detection for SST images. J. Atmos. Oceanogr. Tech. 12, 821–829.

Chao, Y., Gangopadhyay, A., Bryan, F.O., Holland, W.R., 1996. Modeling the Gulf Stream system: how far from reality?. Geophys. Res. Lett. 23, 3155–3158.

Cornillion, P., 1986. The effect of the New England Seamounts on Gulf Stream meandering as observed from satellite IR images. J. Phys. Oceanogr. 16, 386–389.

da Silva, A.M., Young, C.C., Levitus, S., 1994a. Atlas of Surface Marine Data 1994. Algorithms and Procedures. NOAA Atlas NESDIS 6 vol. 1 US Department of Commerce, NOAA, NESDIS, 83 p.

da Silva, A.M., Young, C.C., Levitus, S., 1994b. Atlas of Surface Marine Data 1994. Anomalies of Heat and Momentum Fluxes. NOAA Atlas NESDIS 8 vol. 3 US Department of Commerce, NOAA, NESDIS, 413 p.

Dietrich, G., Kalle, K., Krauss, K., Siedler, G., 1980. General Oceanography, An Introduction. 2nd edn. Wiley, New York, 626 p.

Dengg, J., Beckmann, A., Gerdes, R., 1996. The Gulf Stream separation problem. In: Krauss, W. (Ed.), The Warmwatersphere of the North Atlantic Ocean. Gebr. Borntraeqer, Berlin, pp. 253–290.

DYNAMO, 1997. Dynamics of North Atlantic Models: Simulation and assimilation with high resolution models. Rep. 294, Institut für Meereskunde an der Universität Kiel, Kiel, Germany, 333 p.

European Centre for Medium-range Weather Forecasts (ECMWF), 1994. The Description of the ECMWF/WCRP Level III — A Global Atmospheric Data Archive. ECMWF, Reading/Berkshire, UK, 72 p.

European Centre for Medium-range Weather Forecasts (ECMWF), 1995. User Guide to ECMWF Products, Meteorological Bulletin M3.2. ECMWF, Reading/Berkshire, UK, 71 p.

Fox, D.N., Carnes, M.R., Mitchell, J.L., 1992. Characterizing major frontal systems: a nowcast/forecast system for the Northwest Atlantic. Oceanography 5, 49–54.

Fox, D.N., Carnes, M.R., Mitchell, J.L., 1993. Circulation model experiments of the Gulf Stream using satellite derived fields, NRL FR 7323-92-9412. Nav. Res. Lab., Stennis Space Center, MS, 45 p.

Fratantoni, D.M., 1996. On the pathways and mechanisms of upper-ocean mass transport in the tropical Atlantic Ocean. PhD thesis, The University of Miami, Miami, FL, 247 p.

Fratantoni, D.M., Johns, W.E., Townsend, T.L., 1995. Rings of the North Brazil Current: their structure and behavior inferred from observations and a numerical simulation. J. Geophys. Res. 100, 10633–10654.

Gallacher, P.C., Hogan, P.J., 1998. Hydrodynamical dispersion of dredged materials sequestered on the abyssal seafloor. J. Mar. Syst. 14, 305–318.

Gibson, R., Kållberg, P., Uppala, S., 1996. The ECMWF re-analysis (ERA) project. ECMWF Newslett. 73, 7–17.

Gibson, J.K., Kållberg, P., Uppala, S., Hernandez, A., Nomura, A., Serrano, E., 1997. ECMWF Re-analysis Project Report Series: 1. ERA Description. ECMWF, Reading/Berkshire, UK, 71 p.

Halkin, D., Rossby, H.T., 1985. The structure and transport of the Gulf Stream at 73°W. J. Phys. Oceanogr. 15, 1439–1452.

Hallock, Z.R., Mitchell, J.L., Thompson, J.D., 1989. Sea surface topographic variability near the New England Seamounts: an intercomparison among in situ observations, numerical simulations, and Geosat altimetry from the Regional Energetics Experiment. J. Geophys. Res. 94, 8021–8028.

Hallock, Z.R., Teague, W.J., Thompson, J.D., 1991. A comparison of observed and modeled sea surface topographic time series near the New England Seamounts. J. Geophys. Res. 96, 12635–12644.

Heburn, G.W., 1994. The dynamics of the seasonal variability of the western Mediterranean circulation. In: La Violette, P.E. (Ed.), Seasonal and Interannual Variability of the Western Mediterranean Sea, Coastal Estuarine Stud. 46 AGU, Washington, DC, pp. 249–285.

Hellerman, S., Rosenstein, M., 1983. Normal monthly wind stress over the world ocean with error estimates. J. Phys. Oceanogr. 13, 1093–1104.

Hockney, R.W., 1968. Formation and stability of virtual electrodes in a cylinder. J. Appl. Phys. 39, 4166–4170.

Hockney, R.W., 1970. The potential calculation and some applications. Methods Comput. Phys. 9, 135–211.

Hogan, P.J., Hurlburt, H.E., Jacobs, G.A., Wallcraft, A.J., Teague, W.J., Mitchell, J.L., 1992. Simulation of GEOSAT, TOPEX/Poseidon, and ERS-1 altimeter data from a 1/8° Pacific Ocean model: effects of space–time resolution on mesoscale sea surface height variability. Mar. Technol. Soc. J. 26 (2), 98–107.

Hogg, N.G., 1992. On the transport of the Gulf Stream between Cape Hatteras and the Grand Banks. Deep-Sea Res. 39, 1231–1246.

Holland, W.R., Lin, L.B., 1975. On the generation of mesoscale eddies and their contribution to the oceanic general circulation: I. A preliminary numerical experiment. J. Phys. Oceanogr. 5, 642–657.

Hurlburt, H.E., Metzger, E.J., 1998. Bifurcation of the Kuroshio Extension at the Shatsky Rise. J. Geophys. Res. 103, 7549–7566.

Hurlburt, H.E., Thompson, J.D., 1980. A numerical study of Loop Current intrusions and eddy-shedding. J. Phys. Oceanogr. 10, 1611–1651.

Hurlburt, H.E., Thompson, J.D., 1982. The dynamics of the Loop Current and shed eddies in a numerical model of the Gulf of Mexico. In: Nihoul, J.C.J. (Ed.), Hydrodynamics of Semi-Enclosed Seas. Elsevier, New York, pp. 243–297.

Hurlburt, H.E., Thompson, J.D., 1984. Preliminary results from a numerical study of the New England Seamount Chain influence on the Gulf Stream. In: Holloway, G., West, B.J. (Eds.), Predictability of Fluid Motions. Am. Inst. of Phys., College Park, MD, pp. 489–504.

Hurlburt, H.E., Carnes, M.R., Fox, D.N., Metzger, E.J., Smedstad, O.M., Wallcraft, A.J., 1996a. Eddy-resolving ocean modeling and prediction in the Pacific Ocean with assimilation of satellite altimeter and IR data. Acts du Colloque Oceanographie Operationelle et Observation Spatiale. pp. 105–119, Biarritz, France, Meteo France, CNES, SMF.

Hurlburt, H.E., Wallcraft, A.J., Schmitz, W.J. Jr., Hogan, P.J., Metzger, E.J., 1996b. Dynamics of the Kuroshio/Oyashio current system using eddy-resolving models of the North Pacific Ocean. J. Geophys. Res. 101, 941–976.

Hurlburt, H.E., Wallcraft, A.J., Sirkes, Z., Metzger, E.J., 1992. Modeling of the Global and Pacific Oceans: on the path to eddy-resolving ocean prediction. Oceanography 5, 9–18.

Jacobs, G.A., Hurlburt, H.E., Kindle, J.C., Metzger, E.J., Mitchell, J.L., Teague, W.J., Wallcraft, A.J., 1994. Decade-scale trans-Pacific propagation and warming effects of an El Niño anomaly. Nature 370, 360–363.

Jacobs, G.A., Teague, W.J., Mitchell, J.L., Hurlburt, H.E., 1996. An examination of the North Pacific Ocean in the spectral domain using the Geosat altimeter data and a numerical ocean model. J. Geophys. Res. 101, 1025–1044.

Johns, W.E., Shay, T.J., Bane, J.M., Watts, D.R., 1995. Gulf Stream structure, transport, and recirculation near 68°W. J. Geophys. Res. 100, 817–838.

Kwizak, M., Robert, A.J., 1971. A semi-implicit scheme for grid point atmospheric models of the primitive equations. Mon. Weather Rev. 99, 32–36.

Lai, D., Richardson, P.L., 1977. Distribution and movement of Gulf Stream rings. J. Phys. Oceanogr. 7, 670–683.

Larsen, J.C., 1992. Transport and heat flux of the Florida Current at 27°N derived from cross-stream voltages and profiling data: theory and observations. Philos. Trans. R. Soc. London, A 338, 169–236.

Lee, H., Glenn, S.M., Haidvogel, D.B., 1997. A Gulf Stream synthetic geoid for the TOPEX altimeter. J. Atmos. Oceanogr. Tech., (submitted).

Lee, T.N., Johns, W.E., Zantopp, R.J., Fillenbaum, E.R., 1996. Moored observations of Western Boundary Current variability and thermocline circulation at 26.5°N in the subtropical North Atlantic. J. Phys. Oceanogr. 26, 962–983.

Levitus, S., 1982. Climatological atlas of the world ocean, NOAA Prof. Pap. 13. US Govt. Print. Off., Washington, DC, 173 p.

Luther, M.E., O'Brien, J.J., 1985. A model of the seasonal circulation in the Arabian Sea forced by observed winds. Prog. Oceanogr. 14, 353–385.

Mauritzen, C., 1993. A study of the large-scale circulation and water mass formation in the nordic seas and Arctic Ocean, PhD Dissertation, Massachusetts Institute of Technology and Woods Hole Oceanographic Institution, 212 p.

McClean, J.L., Semtner, A.J. Jr., Zlotnicki, V., 1997. Comparisons of mesoscale variability in the Semtner–Chervin 1/4° model, the Los Alamos Parallel Ocean Program 1/6° model, and TOPEX/POSEIDON data. J. Geophys. Res. 102, 25203–25226.

McManus, A.P., Townsend, T.L., Metzger, E.J., 1997. Creation and modification of 1/8° and 1/16°subtropical gyre Atlantic topographies. NRL FR, 7323-95-9626. Nav. Res. Lab, Stennis Space Center, MS, 23 p.

McWilliams, J.C., Flierl, G.R., 1979. On the evolution of isolated, nonlinear vortices. J. Phys. Oceanogr. 9, 1155–1182.

Mesinger, F., Arakawa, A., 1976. Numerical methods used in atmospheric models. GARP Publ. Ser. 17 World Meteorol. Org., Geneva, Switzerland, 64 p.

Metzger, E.J., Hurlburt, H.E., 1996. Coupled dynamics of the South China Sea, the Sulu Sea, and the Pacific Ocean. J. Geophys. Res. 101, 12331–12352.

Metzger, E.J., Hurlburt, H.E., Kindle, J.C., Sirkes, Z., Pringle, J.M., 1992. Hindcasting of wind driven anomalies using a reduced-gravity global ocean model. Mar. Technol. Soc. J. 26 (2), 23–32.

Mitchell, J.L., Teague, W.J., Jacobs, G.A., Hurlburt, H.E., 1996. Kuroshio Extension dynamics from satellite altimetry and a model simulation. J. Geophys. Res. 101, 1045–1058.

Moore, D.R., Wallcraft, A.J., 1998. Formulation of the Navy Layered Ocean Model in spherical coordinates, NRL CR 7323-96-0005. Nav. Res. Lab., Stennis Space Center, MS, 24 p.

Munk, W.H., 1950. On the wind-driven ocean circulation. Journ. Meteorol. 7, 79–93.

Murphy, S.J., Hurlburt, H.E., O'Brien, J.J., 1999. The connectivity of eddy variability in the Caribbean Sea, the Gulf of Mexico, and the Atlantic Ocean. J. Geophys. Res. 104, 1431–1453.

National Oceanic and Atmospheric Administration (NOAA), 1986. ETOP05 digital relief of the surface of the earth, Data Announcement 86-MGG-07, Natl. Geophys. Data Cent., Washington, DC.

Rhines, P.B., Holland, W.R., 1979. A theoretical discussion of eddy-driven mean flows. Dyn. Atmos. Oceans 13, 301–316.

Richardson, P.L., 1985. Average velocity and transport of the Gulf Stream near 55°W. J. Mar. Res. 43, 83–111.

Richardson, P.L., Knauss, J.A., 1971. Gulf Stream and western boundary undercurrent observations at Cape Hatteras. Deep-Sea Res. 18, 1089–1109.

Schmitz, W.J. Jr., 1984. Abyssal eddy kinetic energy in the North Atlantic. J. Mar. Res. 42, 509–536.

Schmitz, W.J. Jr., 1996. On the World Ocean Circulation: Volume I, some global features/North Atlantic circulation. Woods Hole Oceanographic Institution Technical Report WHOI-96-03, 141 p.

Schmitz, W.J. Jr., McCartney, M.S., 1993. On the North Atlantic circulation. Rev. Geophys. 31 (1), 29–49.

Schmitz, W.J. Jr., Richardson, P.L., 1991. On the sources of the Florida Current. Deep-Sea Res. 15 (Suppl. 1), S379–S409.

Schmitz, W.J. Jr., Thompson, J.D., 1993. On the effects of horizontal resolution in a limited-area model of the Gulf Stream system. J. Phys. Oceanogr. 23, 1001–1007.

Shriver, J.F., Hurlburt, H.E., 1997. The contribution of the global thermohaline circulation to the Pacific to Indian Ocean throughflow via Indonesia. J. Geophys. Res. 102, 5491–5511.

Shriver, J.F., Hurlburt, H.E., 1998. The effects of eddies on the global thermohaline circulation and its contribution to the Pacific to Indian Ocean throughflow via Indonesia. J. Geophys. Res, (submitted).

Smedstad, O.M., Fox, D.N., 1994. Assimilation of altimeter data in a 2-layer primitive equation model of the Gulf Stream. J. Phys. Oceanogr. 24, 305–325.

Smedstad, O.M., Fox, D.N., Hurlburt, H.E., Jacobs, G.A., Metzger, E.J., Mitchell, J.L., 1997. Altimeter data assimilation into a 1/8° eddy-resolving model of the Pacific Ocean. J. Meteorol. Soc. Jpn. 75 (1B), 429–444.

Spall, M.A., 1996a. Dynamics of the Gulf Stream/Deep Western Boundary Current crossover, Part I: Entrainment and recirculation. J. Phys. Oceanogr. 26, 2152–2168.

Spall, M.A., 1996b. Dynamics of the Gulf Stream/Deep Western Boundary Current crossover, Part II: Low frequency internal oscillations. J. Phys. Oceanogr. 26, 2169–2182.

Sverdrup, H.E., 1947. Wind-driven currents in a baroclinic ocean; with application to the equatorial currents of the eastern Pacific. Proc. Natl. Acad. Sci. U. S. A. 33, 318–326.

Teague, W.J., Carron, M.J., Hogan, P.J., 1990. A comparison between the generalized digital environmental model and the Levitus climatology. J. Geophys. Res. 95, 7167–7183.

Thompson, J.D., Schmitz, W.J. Jr., 1989. A limited area model of the Gulf Stream: design and initial experiments. J. Phys. Oceanogr. 19, 791–814.

Thompson, J.D., Townsend, T.L., Wallcraft, A.J., Schmitz, W.J. Jr., 1992. Ocean prediction and the Atlantic basin: scientific issues and technical challenges. Oceanography 5, 36–41.

Townsend, T.L., Hurlburt, H.E., Hogan, P.J., 2000. Modeled Sverdrup flow in the North Atlantic from 11 different wind stress climatologies. Dyn. Atmos. Oceans 32, 373–417.

Wallcraft, A.J., 1991. The Navy Layered Ocean Model Users Guide. NOARL Rep. 35 Nav. Res. Lab, Stennis Space Center, MS, 21 p.

Wallcraft, A.J., 1998. A comparison of several scalable programming models. In: O'Keefe, M., Kerr, C. (Eds.), Second International Workshop on Software Engineering and Code Design in Parallel Meteorological and Oceanographic Applications. NASA Conference Publication, GSFC/CP-1998-206860 pp. 183–197.

Wallcraft, A.J., Moore, D.R., 1997. The NRL layered ocean model. Parallel Comput. 23, 2227–2242.

Woodruff, S.D., Slutz, R.J., Jenne, R.L., Steurer, P.M., 1987. A comprehensive ocean–atmosphere data set. Bull. Am. Meteorol. Soc. 68, 1239–1250.